

# Coherent Association of Single Molecules from Single Atoms

A DISSERTATION PRESENTED  
BY  
YICHAO YU  
TO  
THE DEPARTMENT OF PHYSICS

IN PARTIAL FULFILLMENT OF THE REQUIREMENTS  
FOR THE DEGREE OF  
DOCTOR OF PHILOSOPHY  
IN THE SUBJECT OF  
PHYSICS

HARVARD UNIVERSITY  
CAMBRIDGE, MASSACHUSETTS  
MARCH 2021

©2021 – YICHAO YU  
ALL RIGHTS RESERVED.

Thesis advisor: Professor Kang-Kuen Ni

Yichao Yu

# Coherent Association of Single Molecules from Single Atoms

ABSTRACT

# Contents

o	INTRODUCTION	I
1	APPARATUS	2
1.1	Laser Sources . . . . .	2
1.2	Cooling Beams . . . . .	2
1.3	Tweezer and Imaging . . . . .	3
2	COMPUTER CONTROL OF THE EXPERIMENT	4
2.1	Introduction . . . . .	4
2.2	Frontend . . . . .	6
2.3	Backends . . . . .	6
2.4	Automation of Scan . . . . .	7
2.5	Summary and Outlook . . . . .	7
3	RAMAN SIDEBAND COOLING	8
3.1	Introduction . . . . .	8
3.2	Basic Theory . . . . .	10
3.3	Raman Sideband Thermometry . . . . .	14
3.4	Setup . . . . .	15
3.5	Cooling Performance and Challenge with Large Lamb-Dicke Parameter . . . . .	17
3.6	Solution: High Order Sidebands . . . . .	19
3.7	Solution: Simulation Based Optimization . . . . .	21
3.8	Alignment of Raman and OP Beams . . . . .	22
3.9	Implementing Optimized RSC Sequence . . . . .	25
3.10	Cooling Performance . . . . .	28
3.11	Conclusion . . . . .	29
4	INTERACTION OF SINGLE ATOMS	32
4.1	Scattering Length . . . . .	32
4.2	Two Interacting Atoms in Optical Tweezer . . . . .	33
4.3	Interaction Shift Spectroscopy . . . . .	37
4.4	Summary and Outlook . . . . .	37
5	PHOTOASSOCIATION OF SINGLE ATOMS	38
5.1	Introduction . . . . .	38

5.2	Energy Levels . . . . .	39
5.3	Photoassociation Spectroscopy . . . . .	47
6	TWO-PHOTON SPECTROSCOPY OF NaCs GROUND STATE	51
6.1	Introduction . . . . .	51
6.2	Weakly bound NaCs Ground States . . . . .	53
6.3	Angular momentum Coupling in $N = 2$ Ground State . . . . .	54
7	COHERENT OPTICAL CREATION OF NaCs MOLECULE	56
7.1	Introduction . . . . .	57
7.2	Raman Transition Beyond Three-Level Model . . . . .	57
7.3	STIRAP . . . . .	65
7.4	States Selection . . . . .	75
7.5	Raman Transfer Results . . . . .	79
7.6	Conclusion . . . . .	79
8	CONCLUSION	80
	APPENDIX A COMPUTER CONTROL HARDWARE SPECIFICATION	81
	APPENDIX B FULL RAMAN SIDEBAND COOLING SEQUENCE	82
	REFERENCES	90



# Acknowledgments

,

# 0

## Introduction



# 1

## Apparatus

### 1.1 LASER SOURCES

### 1.2 COOLING BEAMS

(MOT, OP, Raman )

### 1.3 TWEEZER AND IMAGING

# 2

## Computer Control of the Experiment

### 2.1 INTRODUCTION

The experiment sequence and data taking is managed by computers. In addition to controlling the timing and the actions during a sequence, the computer control system is also the main interface between the people running the experiment (the user), the data and the hardware performing the manipulation and measurements. Because of its central role in the experiment, it has to satisfy many

requirements so that the daily operation of the lab can be performed smoothly and reliably.

1. Full control and utilization of hardware.

The control system is a layer in between the the user and the hardware and will abstract and manage the hardware on behave of the user. However, the abstraction must still allow the user to take advantage of the full capability of the hardware, e.g. output resolution, timing accuracy etc.. This is because there is usually little margin between the capability of the hardware and the requirement in the experiment as the specification of the hardware is often selected based on the requirement to begin with.

2. Usability for all lab members.

The lab is operated by users with specialty in physics rather than computer science. Although some basic knowledge of computer programming is required for operating the experiment as well as analysing data, the computer control system must be fully usable for people without any experience in building complex software systems.

The inevitable complexity of the system must be fully hidden from the user for normal operations although more direct control may still be allowed in certain cases.

3. Modeling of the sequence and scan.

As an important special case of usability, the computer control system must provide a model for each tasks closed to the users' mental model. More concretely, this means creating abstraction for concepts typically used to describe the task and allow operation on these abstractions matching the users' expectation. We will talk about concrete examples of this requirements in section 2.2 regarding the sequence frontend and section 2.4 regarding scan automation.

4. Reproducibility.

When exploring something new in the experiment, trial and error is the standard method and troubleshooting is a major part of the process. The ability to do this effectively requires a high degree of reproducibility of all the result. While it is impossible and also not the job of the computer control system to eliminate all the fluctuation and noise in the experiment, it should not add to the randomness of the system. With few exceptions, identical user input should produce identical output from the control system.

5. Version control.

As a variation of the reproducibility requirement and also built on top of it, we must be able to revert to a previous software configuration at a later time in order to reproduce and

double-check an earlier result. The use of a proper version control system on the settings and code for the computer control system can allow this with additional features including easy visualization of setting change and parallel development of code by multiple users.

The design of the computer control system is mainly guided by these requirements and we will go into more detail as we describe each part of the system. Section 2.2 will cover the frontend of the system which is used by the user directly to specify an experimental sequence. Section 2.3 will discuss the support for various hardware backends used to run a sequence. After that, section 2.4 describes how multiple sequences can be put together to form a scan and we will talk about some planned update to the system in section 2.5.

## 2.2 FRONTEND

(Abstraction) (Backward compatibility) (Flexibility) (Text based/version control friendly)

## 2.3 BACKENDS

(communication protocol) (IR)

### 2.3.1 FPGA BACKEND

(clock generation) (pulse merging) (compression)

### 2.3.2 NIDAQ BACKEND

(Variable clock)

### 2.3.3 USRP BACKEND

(SIMD)

### 2.4 AUTOMATION OF SCAN

(Scan requirement) (Combination of scans) (Scope/nested structure)

### 2.5 SUMMARY AND OUTLOOK

(new backend/SPCM) (native code generation, auto vectorization) (dynamic logic and dependency tracking/optimization)

# 3

## Raman Sideband Cooling

### 3.1 INTRODUCTION

(In order to achieve full quantum control on molecules, we need to control atoms first.) (An example of such control) (Motional degrees of freedom) (PGC cools to ...) (RSC to further cool.)



**Figure 3.1:** Single Na atom Raman sideband cooling scheme. The Raman transitions couples  $|2, 2; n\rangle$  and  $|1, 1; n + \Delta n\rangle$  through the intermediate states  $|e_i\rangle$  in the  $3^2P_{3/2}$  electronic states. The transitions have a one-photon detuning  $\Delta_i \approx 75$  GHz. Two-photon detuning,  $\delta$ , is defined relative to the  $\Delta n = 0$  carrier transition. For optical pumping, we use two  $\sigma^+$  polarized transitions, one to pump the atom state out of  $|1, 1\rangle$  via  $3^2P_{3/2}$  and one to pump atoms out of  $|2, 1\rangle$  via  $3^2P_{1/2}$  to minimize heating of the  $|2, 2\rangle$  state.



## 3.2 BASIC THEORY

The relevant energy diagram and the laser frequencies for RSC are shown in Fig. 3.1. We approximate the trapping potential using a harmonic oscillator. Since this is a separable potential, we can use only the 1D motional state  $|n\rangle$  and the result can be easily generalized to the full 3D system.

The cooling sequence consists of two types of pulses. First, a Raman pulse drives the atom to a different hyperfine state while simultaneously reduces the motional energy of the atom. The optical pumping (OP) pulse afterwards then reset the hyperfine state of the atom and reduce the entropy of the system. This sequence is then repeated until the system reaches the ground motional state where there is no more motional energy to be taken out of the system via the Raman pulse. In this section, we will discuss the theory of each types of pulses individually. We will cover how the pulses affect cooling performance in section 3.5.

### 3.2.1 RAMAN TRANSITION

As shown in Fig. 3.1, the cooling sequence starts with the sodium atom in the  $|s_1\rangle \equiv |2, 2\rangle$  hyperfine state, and a Raman transition is used to drive the atom to the  $|s_2\rangle \equiv |1, 1\rangle$  state, where  $|F, m_F\rangle$  denotes the  $F$  and  $m_F$  quantum number for the sodium atom. The full Rabi frequency for such a transition is given by

$$\Omega_R^0 = \sum_i \frac{\Omega_{1i}\Omega_{2i}^*}{2\Delta_i} \quad (3.1)$$

where the sum is over all the coupled excited states,  $\Omega_{ai} \equiv \langle a | \mathbf{d} \cdot \mathbf{E}_a | e_i \rangle$  is the single photon Rabi frequency between  $|a\rangle$  and  $|e_i\rangle$  and  $\Delta_i$  is the single photon detuning from excited state  $|e_i\rangle$ .

In order to account for the motional degrees of freedom, we need to include the spatial wavefunction of the atom and light into account. As mentioned above, we approximate the atomic motional wavefunction by the harmonic oscillator eigenstates  $|n\rangle$ . Coupling between states different  $n$  states from the Raman transition is allowed due to the recoil from the Raman lasers, which corresponds to a spacial phase imprinting of  $e^{i\Delta\mathbf{k} \cdot \mathbf{x}}$  where  $\Delta\mathbf{k}$  is the wavevector difference between the two Raman beams. Using the creation ( $\hat{a}^\dagger$ ) and annihilation ( $\hat{a}$ ) operators and the relation  $\mathbf{x} = x_0(\hat{a} + \hat{a}^\dagger)$  where  $x_0 = \sqrt{\hbar/2m\omega}$  is the harmonic oscillator length, the phase factor can be expressed as  $e^{i\eta^R(\hat{a} + \hat{a}^\dagger)}$  where  $\eta^R \equiv \Delta\mathbf{k} \cdot \mathbf{x}_0$  is the Lamb-Dicke parameter for the Raman transition. The matrix element between motional state  $|n\rangle$  and  $|n'\rangle$  is therefore,

$$M_{n,n'} = \langle n | e^{i\eta^R(\hat{a} + \hat{a}^\dagger)} | n' \rangle$$

and the final Raman Rabi frequency between motional states  $n$  and  $n'$  is given by,

$$\Omega_R^{n,n'} = M_{n,n'} \Omega_R^0$$

For  $n = n'$ , this is called a carrier transition and the others are called sideband transitions. If the final state is higher than the initial one, i.e.  $n' > n$ , it is a heating sideband. Likewise, transitions with  $n' < n$  are cooling sidebands.

A closed form result for  $\mathcal{M}_{n,n'}$  is given in ,

$$\mathcal{M}_{n,n'} = e^{(\eta^R)^2/2} \sqrt{\frac{n_{<}!}{n_{>}!}} (\eta^R)^{|n-n'|} L_{n_{<}}^{|n-n'|} \left( (\eta^R)^2 \right)$$

where  $n_{<}$  and  $n_{>}$  are the lesser and greater, respectively, of  $n$  and  $n'$ , and  $L_n^\alpha$  is the generalized Laguerre polynomial,

$$L_n^\alpha(x) \equiv \sum_{m=0}^n (-1)^m \binom{n+\alpha}{n-m} \frac{x^m}{m!}$$

An important limit is the so-called Lamb-Dicke (LD) regime defined by  $(\eta^R)^2(2n+1) \ll 1$ . In this case, we can approximate the phase factor in leading order of  $\eta^R$ ,

$$e^{i\eta^R(\hat{a}+\hat{a}^\dagger)} \approx 1 + i\eta^R(\hat{a} + \hat{a}^\dagger)$$

and the matrix element

$$\mathcal{M}_{n,n'} \approx \delta_{n,n'} + i\eta^R \sqrt{n+1} \delta_{n+1,n'} + i\eta^R \sqrt{n} \delta_{n,n'+1}$$

the three terms corresponds to the carrier ( $n' = n$ ), the first order heating sideband ( $n' = n+1$ ) and the first order cooling sideband ( $n' = n-1$ ) with corresponding strength  $1$ ,  $\eta^R \sqrt{n+1}$  and  $\eta^R \sqrt{n}$ . We can clearly see from this approximation that the coupling to other motional state is stronger for a larger  $\eta^R$  and higher motional quantum number  $n$ . We will discuss this effect outside the LD regime and its implication on the cooling performance in more detail in section 3.5.

## SCATTERING FROM RAMAN BEAMS

In addition to driving the Raman transition, the Raman beams can also cause scattering. The rate of the scattering is <sup>\*</sup>,

$$\Gamma = \sum_i \frac{\Gamma_{ei} \Omega_{li}^2}{4\Delta_i^2}$$

where  $\Gamma_{ei}$  is the linewidth of the excited state  $|e_i\rangle$ . Together with (3.1), we see that approximately  $\Gamma/\Omega_R \propto 1/\Delta$  so a larger detuning should be used in order to reduce the scattering during RSC.

### 3.2.2 OPTICAL PUMPING

Driving the system on a cooling sideband with Raman transition can reduce the motional energy of the atom. However, this is a fully coherent process that does not reduce the system entropy and is not really “cooling” the system or achieving better control on the quantum state of the system. Instead, quantum state control is achieved in the RSC via the OP pulse. The initial hyperfine state  $|2, 2\rangle$  is a stretched state so it is the state the system naturally ends up in when  $\sigma^+$  light is applied. However, if this is done using scattering from a  $F = 2$  to  $F' = 3$  transition, the OP beam will allow continuous photon cycle between the  $|2, 2\rangle$  and the  $|3', 3\rangle$  causing unnecessary motional heating during OP. Therefore, the OP must be done on a  $F = 2$  to  $F' = 2$  transition. Unfortunately, for Na, the corresponding transition from  $3^2S_{1/2}$  to  $3^2P_{3/2}$  that is used for the MOT is not useable due to

---

<sup>\*</sup>Here we assume that each Raman beam only couples to their respective ground states. Including coupling to the other ground state increases the scattering rate but does not change the scaling with detuning.

the small energy difference of 60MHz (or 6 line widths) between the  $F = 2$  and  $F = 3$  states <sup>Steck</sup>.

Instead, we must use the sodium D1 line, i.e.  $3^2S_{1/2}$  to  $3^2P_{1/2}$  transition, which lacks a  $F = 3$  excited state. The D1 light with  $\sigma^+$  polarization is only used to pump atoms from  $F = 2$  states (in particular  $|2, 1\rangle$  which is populated during the OP process). Since the goal of the OP pulse is to clear the atom population in all states but  $|2, 2\rangle$ , the photon cycling is not a concern for  $F = 1$  states and the D2 line is used for OP of  $F = 1$  states instead. This also allow us to reuse the MOT light source and simplifies our setup.

### 3.3 RAMAN SIDEBAND THERMOMETRY

From the discussion in section 3.2.1, we see that the strength of the sideband transition depends on the initial motional state as well as the Lamb-Dicke parameter  $\eta^R$  of the atom. This dependency allows us to infer the motional state of the atom by measuring the sideband height, i.e. the so-called sideband thermometry.

In particular, for atom with temperature  $T$ , the probability for the atom to be in motional state  $|n\rangle$  is,

$$p_n = \frac{e^{-n\hbar\omega/k_B T}}{1 - e^{-\hbar\omega/k_B T}}$$

for a Raman pulse with full Rabi frequency  $\Omega_R^0$  and time  $t$ , the peak height for the first order heating (+) and cooling (-) sidebands,

$$h_{\pm} = \sum_{n=0}^{\infty} p_n \sin^2 \left( \frac{\Omega_R^0 t}{2} M_{n,n\pm 1} \right)$$

note that  $p_{n+1} = p_n e^{-\hbar\omega/k_B T}$ ,  $M_{n,n'} = M_{n',n}$  and  $M_{n,-1} = 0$ , we have

$$\begin{aligned}
h_- &= \sum_{n=0}^{\infty} p_n \sin^2 \left( \frac{\Omega_R^0 t}{2} M_{n,n-1} \right) \\
&= e^{-\hbar\omega/k_B T} \sum_{n=1}^{\infty} p_{n-1} \sin^2 \left( \frac{\Omega_R^0 t}{2} M_{n-1,n} \right) \\
&= e^{-\hbar\omega/k_B T} h_+
\end{aligned}$$

Therefore, if we measure the ratio of the cooling and heating sideband heights  $\alpha \equiv h_-/h_+$ , we can calculate the temperature of the atom with  $e^{-\hbar\omega/k_B T} = \alpha$ . The corresponding ground state probability is,

$$\begin{aligned}
p_0 &= \frac{1}{1 - e^{-\hbar\omega/k_B T}} \\
&= \frac{1}{1 - \alpha}
\end{aligned}$$

We will use this to experimentally characterize the performance of the cooling sequence in the following sections.

### 3.4 SETUP

The geometry of all the beams and field involved is shown in Fig. 3.2. In order to make the cooling more efficient and simplify the sideband thermometry, we address the motion along the three principle axis of the tweezer using different pairs of Raman beams. In order to maximize the beam



**Figure 3.2:** Geometry and polarizations of the Raman and optical pumping beams relative to the optical tweezer and bias magnetic field. Raman beams R1 and R4 address the radial  $x$ -mode. R1 and R2 address the radial  $y$ -mode. R3 and R4 address the axial  $z$ -mode, where the beams also couple to radial motion, but this coupling can be neglected when the atoms is cooled to the ground state of motion.

intensity so that a larger single photon detuning can be used while maintaining the same Raman Rabi frequency, we focus the Raman beam onto the single atom with a waist of  $\approx 100\mu\text{m}$ . The maximum powers within each Raman beam are between 1 and 6mW which give us a maximum Raman Rabi frequency of 50 to 200kHz.

We apply an external bias magnetic field of 8.8G parallel to the polarization of the tweezer beam (and orthogonal to the tweezer beam propagation direction). This makes the field orthogonal to the effective magnetic field of the tweezer, which minimizes the vector light shifts [Kaufman et al., Thompson et al.](#). Since the optical pumping beam requires  $\sigma^+$  polarization, it is setup to propagate parallel to the applied magnetic field.

### 3.5 COOLING PERFORMANCE AND CHALLENGE WITH LARGE LAMB-DICKE PARAMETER

RSC is typically performed in the LD regime where the coupling to other motional state is small.

Due to the light mass, short wavelength, limited trap depth and high initial temperature of the sodium atom however, we have to start our RSC sequence outside the LD regime. This creates unique challenges to our experiment. A detailed understanding of the cooling performance is required to understand and overcome these challenges.

The simplest way to estimate the effectiveness of RSC is by keeping track of the average energy of the atom during the cooling sequence. For a typical RSC sequence in the LD regime, all the cooling are done on the strongest first order cooling sideband. The energy removed for atom driven in one Raman pulse is therefore,  $\Delta E_- = \omega$ . In order to reinitialize the hyperfine state, the sodium atom needs to scatter on average 2 photons from the OP pulse which increases the average energy of the driven atom by  $\Delta E_+ = 4\omega_r$ <sup>†</sup> where  $\omega_r \equiv \hbar k^2/2m$  is the recoil energy<sup>Steck</sup> and  $k$  is the OP light wave vector. The heating to cooling ratio in one RSC pulse cycle is therefore,

$$\begin{aligned}\frac{\Delta E_+}{\Delta E_-} &= \frac{2\hbar k^2}{m\omega} = 4k^2 x_0^2 \\ &= 4(\eta^{OP})^2\end{aligned}$$

where  $\eta^{OP} \equiv kx_0$  is the Lamb-Dicke parameter for OP. Therefore, in order to achieve net cooling, we need  $(\eta^{OP})^2 < 0.25$ . In 3D with cooling along multiple axis with different trapping frequency

---

<sup>†</sup>The factor of 4 comes from 2 absorbed photons and 2 reemitted photons.





**Figure 3.3:** Optical pumping motional-state redistribution and Raman coupling for large LD parameters for the axial direction ( $z$ ). The range plotted covers 95% of the initial thermal distribution. (A) Motional state distribution after one OP cycle for different initial states motion,  $n_{init}$ . Due to photon-recoil and the large LD parameter,  $\eta_z^{OP} = 0.55$ , there is a high probability of  $n$  changing. (B) Matrix elements for Raman transition on the first order cooling sideband deviate from  $\sqrt{n}$  scaling with multiple minima.

(and therefore different  $\eta^{OP}$ ), the  $(\eta^{OP})^2$  in the requirement is replaced by a weighted average of different axis depending on the frequency each axis is cooled in the sequence.

In our experiment, the OP Lamb-Dicke parameters are  $\eta_x^{OP}, \eta_y^{OP}, \eta_z^{OP} = 0.25, 0.25, 0.55$ . Based on the metric above, any cooling sequences that have fewer than 78% cooling pulse for  $z$  (axial) axis, which is generally the case, should have a net cooling effect. This, however, does not guarantee cooling into the ground motional state, nor does it fully characterize the efficiency of the cooling sequence since the averaging hides a few critical aspect of having a large Lamb-Dicke parameter.

One of the important effects can be seen in Fig. 3.3A showing the motional state distribution after one OP cycle for different initial motional states  $n_{init}$ . Although the average heating is fixed at  $4\omega_r$ , independent of  $n_{init}$ , the spread or the uncertainty of  $n$  after the OP is significantly higher for high  $n_{init}$ . This effect significantly increases the difficulty in controlling the state during the RSC sequence. It can negatively impact the cooling performance and may lead to increased loss during

cooling due to atom escaping to higher motional states.

The other important effect is the dependency of matrix element  $M_{n,n+1}$  on the motional level  $n$ . While this dependency is not a new effect, since the  $\sqrt{n}$  dependency on the cooling sideband strength exist even in the LD regime and must be taken into account with pulse time variation to achieve efficient cooling, the high Lamb-Dicke parameter adds even more complications. As shown in Fig. 3.3B, rather than a simple  $\sqrt{n}$  dependency, it is a non-monotonic function and more importantly has multiple minima, so-called “dead-zone”, within the range of motional states we are interested in. The coupling strength for states in the dead-zones can be reduced by more than ten times which can significant affect the efficiency of the cooling pulse and even makes it virtually impossible to drive Raman transitions on atoms in these states in order to cool them further. A cooling sequence can therefore accumulate pupolations in the dead-zones rather than the ground state. Their small coupling strength also reduce their signal level during Raman sideband spectroscopy making these states nearly invisible to sideband thermometry which further complicates the optimization of the cooling sequence.

### 3.6 SOLUTION: HIGH ORDER SIDEBANDS

The main solution to the issues related to the large Lamb-Dicke parameter is in fact the large Lamb-Dicke parameter itself. The increased coupling to other motional state for large Lamb-Dicke parameter and high motional states applies not only to  $|\Delta n| = 1$  but to higher  $\Delta n$  as well. Fig. 3.4 shows the coupling to higher order cooling sidebands which all have comparable strengths as the first order



**Figure 3.4:** Matrix elements for Raman transition including high order sidebands. During cooling, we utilize the fact that high motional states couple most effectively to sidebands with large  $|\Delta n|$  in order to overcome the issue with variation and dead zone in the coupling strengths.

sidebands in different ranges of motional states.

Because of this, it is now possible, and in some cases preferred, to apply Raman cooling pulse on the higher order sidebands instead of only the first order one. These pulses reduce more energy from the system per pulse which directly improves the cooling to heating ratio and allows better control on the motional state given the uncertainty after an OP pulse. More importantly, depending on the motional level, there is always a sideband order with significant coupling strength that can be used to cool it, therefore completely removing the coupling dead-zones. Moreover, by using each sideband orders only near their coupling maxima, the coupling strength variation is also greatly reduced which removes the need to vary the pulse times for all but the pulses on the first order sideband.



**Figure 3.5:** Schematic of the cooling pulse sequence. The tweezer is strobed at 3 MHz to reduce light shifts during optical pumping<sup>Hutzler et al.</sup>. Each cooling cycle consists of 8 sideband pulses. The four axial pulses address two sideband orders. The two pulses in each radial direction either address  $\Delta n = -2$  and  $\Delta n = -1$  or have different durations to drive  $\Delta n = -1$ , at the end of the cooling sequence when most of the population is below  $n = 3$ . The Raman cooling and spectroscopy pulses have Blackman envelopes<sup>Kasevich & Chu</sup> to reduce off-resonant coupling, while the measurement Rabi pulses in Fig. 3.7 have square envelopes to simplify analysis.

### 3.7 SOLUTION: SIMULATION BASED OPTIMIZATION

The change in cooling technique by including higher order sidebands, however, does not remove the effect of coupling variation on the sideband thermometry. If a non-thermal distribution of motional states is produced by the cooling sequence, the ratio of the first order sideband height still cannot be trusted to calculate the temperature or the ground state probability. Including higher order sidebands in the sideband thermometry could in principle give us enough information about the state distribution but doing so for a non-thermal distribution is not easy or reliable. We therefore use a Monte-Carlo simulation to guide our search for the optimal sequence. The simulation includes accurate scattering rate and branching ratios from the tweezer, Raman and OP beams. For

best simulation performance, the atom is assumed to be in a single motional state, i.e. with a certain  $n_x, n_y$  and  $n_z$ , after each Raman or OP step<sup>‡</sup>. It is also assumed that each Raman pulse drives only the intended sideband order, which is a property that needs to be ensured in the experiment (see section 3.9.1). For each cooling sequence simulated, the Raman beam power and frequency, and the OP beam power and polarization purity are varied slightly around the respective expected values in order to confirm the robustness of the sequence against fluctuation in the experiment. Fig. 3.5 demonstrate the resulting optimal sequence from the simulation. In particular, we find that alternating the cooling pulses between two neighboring orders for the axial direction and  $\Delta n = -2$  and  $\Delta n = -1$  for the radial directions eliminates the accumulation of population in motional states with small Raman coupling. The simulation also confirms that setting the coupling strength of each sideband to drive a Rabi  $\pi$ -pulse corresponding to the maximum matrix element motional state (i.e. the maxima in Fig. 3.4) yields efficient cooling, initially, as we expected from section 3.6. The efficiency of cooling on higher-order sidebands diminishes as the atom approaches the ground state, so the final cycles utilize only the  $\Delta n = -1$  sideband while alternating between the three axes.

### 3.8 ALIGNMENT OF RAMAN AND OP BEAMS

Due to small waist of the Raman beam, it is important to align the Raman beam to the single atom with high precision in order to maximize the Raman Rabi frequency as well as minimizing the intensity fluctuation of the Raman beam experienced by the atom due to pointing instability. Such

---

<sup>‡</sup>This assumes no coherence between different motional state, which is the case as long as each Raman pulses are separated from each other by OP pulses.

precision cannot easily be achieved using external reference and must be done by using the single atom itself as the alignment target.

In our experiment, we have developed two different methods to align or verify the alignment of the Raman beams, both relying on the scattering from the Raman beams. For initial alignment, or when the beam position is off-center by more than a beam waist, we couple resonant Sodium D<sub>2</sub> light into the Raman beam path in order to enhance the scattering rate. The coarse alignment is done based on maximizing depletion and displacement of the MOT due to radiation pressure. After that, the fine alignment of the Raman beam is done by reducing the power in the Raman beam path and maximizing the heating effect on the single atom. When the Raman beam is focused on the tweezer position, we can observe a depletion of the single atom live loading signal while the MOT is not affected as significantly. This process is then repeated with lower power in the Raman beam path until the desired position sensitivity is reached.

In order to verify the alignment of the tweezer without any physical change to the beam path, we use a second method to calibrate the single photon Rabi frequency of the Raman light. This method requires a working OP to initialize the spin state of the atom so it is less convenient for aligning from scratch. To use this method, the atom is first loaded in the tweezer and initialized in the  $|2, 2\rangle$  state. We then turn on a single Raman beam at maximum power for a variable length of time. The off resonance scattering from the Raman beam will cause the spin state of the atom to change and the population in  $F = 1$  state is measured by removing the  $F = 2$  population using a pushout pulse. The rate of the spin change is fitted to a theory model to derive the Rabi frequency of the Raman light. This measurement shows that the Rabi frequencies for the Raman beams are ... . We can

also calculate the scattering rate from the Raman beams to be ... which corresponds to a total of ... scattering event on average during the whole cooling sequence and should not be a limiting factor for the cooling performance.

The OP beam has a much larger waist ( $\approx 1\text{mm}$ ) and therefore require less alignment in the beam position. However, in order to take advantage of the dark state optical pumping and minimize unnecessary scattering for atoms in the  $|2, 2\rangle$  state, the OP beam need to have a pure  $\sigma^+$  polarization. This requires the OP beam to propagate parallel to the magnetic field in addition to having the correct circular polarization. The alignment is done by minimizing “depumping” of the atom spin state caused by the OP beam, similar to the technique we used to calibrate the Raman beam Rabi frequency. After the atom is initialized in the  $|2, 2\rangle$  state, we turn on the D1 OP light for a certain time which should not address the atom when perfectly aligned. The misalignment of the beam, however, will cause the atom to scatter from the OP beam and change to  $F = 1$  state, i.e. “depumped”, with certain probability. We then change the alignment of the beam an minimize the depumping rate. Due to a similar requirement for Cesium OP, the probagation direction of the OP beam for Sodium and Cesium are aligned to each other by overlapping them using mechanical target to better than  $0.08^\circ$  first before the magnetic field direction is aligned to the OP beams by minimizing depumping. For polarization alignment, we first clean up the linear polarization of the light using a Thorlabs nanoparticle linear film polarizer with better than  $100,000 : 1$  extinction ratio. After that we use both a half waveplate and a quater waveplate to generate a circularly polarized light. We observed that both the polarization cleanup and the half waveplate is necessary to obtain the best polarization alignment in order to compensate for the polarization fluctuation caused by the fiber as

well as the birefringence of the optics and windows within the OP beam path. After alignment, the OP intensity is calibrated by measuring the OP rate for atom prepared in  $|2, 1\rangle$  state using Raman transitions<sup>§</sup>. From this measurement we determined that the purity of the OP polarization to be ...

Other than the alignment procedure above, we have also observed that reflection of the OP beam can contribute significantly to the polarization impurity and must be avoided. In particular, since the Raman beam  $R_1$  counter propagate with the OP beam, it is possible for the OP beam to be coupled into the Raman fiber and then retro-reflected to be focused onto the atom through the Raman beam path at a wrong polarization. Since the Raman beam size is much smaller, we have observed as much as 3% polarization impurity caused by this mechanism despite only a small amount of power being reflected. This issue, along with other reflections, are reduced by avoiding optics with normal incident on the exit path of the OP beam as well as changing the propagation direction of the  $R_1$  Raman beam to have a small angle with the OP beam which reduces the OP power coupled into the Raman beam fiber.

### 3.9 IMPLEMENTING OPTIMIZED RSC SEQUENCE

In order to achieve the optimal cooling performance, a few more considerations are important for implementing the sequence from section 3.7.

---

<sup>§</sup>One from  $|2, 2\rangle$  to  $|1, 1\rangle$  and a second one from  $|1, 1\rangle$  to  $|2, 1\rangle$ .



### 3.9.1 PULSE SHAPING

In order to achieve optimal performance from the cooling sequence, it is important to accurately drive the intended sideband order. In fact, in the absence of undesired scattering, the frequency resolution of the Raman transition limits the lowest achievable temperature. This is particularly important when driving the first order cooling sidebands since any coupling to the carrier may change the spin state of the atom without removing any motional energy therefore causing a net heating effect after the OP pulse.

The obvious way to achieve this is to narrow the linewidth of the Raman transition, e.g. by using a lower power or Raman Rabi frequency. However, reducing the linewidth of the transition also increases the susceptibility to resonance fluctuation. Therefore the desired solution is to reduce the off-resonance coupling of the Raman beam for large detuning while increasing or maintaining the coupling for small detuning. We achieve this by using a Blackman pulse shape for the Raman transition.<sup>¶</sup>

### 3.9.2 CALIBRATION

The Raman sideband frequencies are calibrated by measuring the Raman spectrum before cooling (an example of which is shown in the initial spectrum in Fig. 3.6). However, since high sideband orders are mainly used to cool atoms in high motional state, the resonance frequency for these side-

---

<sup>¶</sup>While more complex pulses can be constructed to achieve a even sharper detuning cutoff, such pulses generally significantly increase the pulse time and can cause more heating during cooling due to scattering and other heating mechanisms. The Blackman pulse we use offers a balance between the pulse time and off-resonance coupling reduction.

band are not equal spacing anymore due to the anharmonicity of the trap. In order to estimate the effect on the sideband frequencies, we can define anharmonicity as  $A_{i,n} = (E_{i,n+1} - E_{i,n})/h - \omega_i/(2\pi)$  for each trap axis  $i$ , and calculated from the quartic term of the optical tweezers via perturbation theory. In the paraxial approximation, we find  $A_{i,n} = \frac{-3n\hbar}{4\pi m d_i^2}$ , where  $d_i$  equals the beam radius for the radial directions and  $d_z \approx \pi w_{0,x} w_{0,y} / \lambda_{\text{trap}}$ . Numerically,  $\{A_{x,n}, A_{y,n}, A_{z,n}\} = \{-1.4, -1.4, -0.16\}n$  kHz. For the states addressed by high order sidebands, this broadens and shifts high-order sidebands due to the  $n$ -dependence of the transitions.

To mitigate this, we calibrate the frequency of each sideband order individually at the initial temperature. However, since the first order sideband is mainly used to cool atoms that are closed to the ground state, their resonance frequency is recalibrated using partially cooled atoms after the initial calibration. The use of high Rabi frequency and Blackman pulse shape also reduces the effect of anharmonicity by broadening the spectrum as much as possible.

Although we can calibrate the single photon Rabi frequency of the Raman beams from the scattering rate (section 3.8), we also calibrate the Raman Rabi frequency on the carrier and different sideband orders. This offers a more direct and sensitive measurement for the cooling sequence parameter. Unlike resonance frequency, the anharmonicity only has a second order effect on the Rabi frequency and is therefore ignored. The calibration measures only the carrier and first order heating sideband which has the highest signal after cooling (an example of which is shown in the cooled Rabi flopping signal in Fig. 3.7). The Raman Rabi frequencies measured on these two transitions are used to calculate the full Rabi frequency  $\Omega_R^0$  and the Lamb-Dicke parameter, which are in-turn used to calculate the Rabi frequency on other sideband orders.



**Figure 3.6:** Raman sideband spectra for (A)  $x$ , (B)  $y$ , (C)  $z$  axis before (red circle) and after (blue square) applying Raman sideband cooling sequence. The height of the cooling sidebands (positive detuning) are strongly suppressed after cooling which suggests most of the atoms are cooled to the motional ground state in the trap.

Since the final calibration of both the Raman Rabi frequency and resonance requires a working cooling sequence, when optimizing the sequence from scratch, the calibration process is applied iteratively as the cooling performance is improved.

### 3.10 COOLING PERFORMANCE

The full sequence including calibrated parameters can be found in appendix B.

3.6 3.7

### 3.11 CONCLUSION

(other systems)

---

**Figure 3.7 (following page):** Rabi flopping on radial axis  $x$  (A) carrier and (B)  $\Delta n_x = 1$  sideband, radial axis  $y$  (C) carrier and (D)  $\Delta n_x = 1$  sideband, axial axis  $z$  (E) carrier and (F)  $\Delta n_x = 1$  sideband, before (red circle) and after (blue square) Raman sideband cooling.

Solid lines (both red and blue) in all plots are fits to a Rabi-flopping that includes a thermal distribution of motional states [Meekhof et al.](#) as well as off-resonant scattering from the Raman beams.

The blue lines correspond to a ground state probability of (A-D) 98.1% along radial axis and (E-F) 95% along the axial axis after cooling. The red lines correspond to a thermal distribution of 80  $\mu$ K before RSC. The horizontal dashed lines in all the plots correspond to the 4 % probability of imaging loss.

The green dashed line in (F) includes the additional decoherence due to a fluctuation of the hyperfine splitting of magnitude 3 kHz. We see that the decoherence effect is strongest for the post-cooling data on the axial  $\Delta n_z = 1$  sideband where the Rabi frequency is the lowest.

Figure 3.7: (continued)



# 4

## Interaction of Single Atoms

### 4.1 SCATTERING LENGTH

(Importance/relation with binding energy etc.)

## 4.2 TWO INTERACTING ATOMS IN OPTICAL TWEEZER

The Hamiltonian for two atoms in an harmonic potential with interaction is,

$$H = \sum_{i=x,y,z} \left( \frac{m_1 \omega_{1,i}^2 r_{1,i}^2}{2} + \frac{p_{1,i}^2}{2m_1} \right) + \sum_{i=x,y,z} \left( \frac{m_2 \omega_{2,i}^2 r_{2,i}^2}{2} + \frac{p_{2,i}^2}{2m_2} \right) + V_{int}(\mathbf{r}_1 - \mathbf{r}_2)$$

where  $m_j$  is the mass of the  $j$ -th atom,  $r_{j,i}$ ,  $p_{j,i}$ ,  $\omega_{j,i}$  are the coordinate, momentum and trapping frequency for the  $j$ -th atom along the  $i$ -th axis.  $V_{int}$  is the interaction potential between the two atoms which is only a function of the relative coordinate between the atoms  $\mathbf{r}_1 - \mathbf{r}_2$ .

Since the two atoms experience the same trapping light field, their trapping potential has the same center and the same shape. However, due to the difference in the polarizability between the atoms, the trap depth can be different. Nevertheless, in our experiment, depending on the trapping wavelength, we have  $\omega_{1,i} \approx \omega_{2,i}$  to within 10% to 20% and this is the regime we will mainly focus on in this section.

The interaction potential  $V_{int}$  is the original for the molecular bound states and its exact form will be discussed in chapter 5, 6 and 7. However, since the range of the potential is much smaller than the size of the atomic wavefunction, we can ignore the short range details of the potential and treat it as a contact interaction characterized only by the scattering length  $a$ .

$$V_{int}(\mathbf{r}) = \frac{2\pi\hbar^2 a}{\mu} \delta_{reg}(\mathbf{r})$$

where  $\mu = m_1 m_2 / (m_1 + m_2)$  is the reduced mass and  $\delta_{reg}(\mathbf{r}) \equiv \delta^{(3)}(\mathbf{r}) (\partial/\partial r) r$  is the regularized



delta-function.

In order to calculate the interaction term, we can change from the coordinates for the two individual atoms to the center of mass (COM) and relative coordinates.

$$\begin{aligned} R_i &= \frac{m_1 r_{1,i} + m_2 r_{2,i}}{m_1 + m_2} & r_{rel,i} &= r_{1,i} - r_{2,i} \\ P_i &= p_{1,i} + p_{2,i} & p_{rel,i} &= \frac{m_2 p_{1,i} - m_1 p_{2,i}}{m_1 + m_2} \end{aligned}$$

The corresponding masses and trapping frequencies are,

$$\begin{aligned} M &= m_1 + m_2 & \mu &= \frac{m_1 m_2}{m_1 + m_2} \\ \Omega_i^2 &= \frac{m_1 \omega_{1,i}^2 + m_2 \omega_{2,i}^2}{m_1 + m_2} & \omega_{rel,i}^2 &= \frac{m_2 \omega_{1,i}^2 + m_1 \omega_{2,i}^2}{m_1 + m_2} \end{aligned}$$

and the Hamiltonian can be expressed as,

$$H = \sum_{i=x,y,z} \left( \frac{M \Omega_i^2 R_i^2}{2} + \frac{P_i^2}{2M} \right) + \left[ \sum_{i=x,y,z} \left( \frac{\mu \omega_{rel,i}^2 r_{rel,i}^2}{2} + \frac{p_{rel,i}^2}{2\mu} \right) + V_{int}(\mathbf{r}_{rel}) \right] + \sum_{i=x,y,z} \mu (\omega_{1,i}^2 - \omega_{2,i}^2) R_i r_{rel,i}$$

The first term and the second term only relies on the COM motion and relative motion respectively and can be solved independently. The third term mixes the COM and relative motion and is proportional to the trapping frequency difference. If the trapping frequencies are the same for the two atoms, the third term is 0 and the solution is fully separateable. As mentioned above, since the trapping frequencies for the two atoms are similar, we will assume the mixing term is small and treat it as

a small correction in the calculation.

#### 4.2.1 PERTURBATIVE CALCULATION

For weak interaction, i.e. a small scattering length  $a$ , the effect of the interaction on the energy level can be calculated perturbatively. The result from this calculation is useful for checking the validity of the full calculation, as well as providing an intuitive understanding of the shift and its dependency on different parameters.

For simplicity, we will assume all the trapping frequencies are the same, i.e.  $\omega_{1,i} = \omega_{2,i} = \omega_{rel,i} = \Omega_i = \omega_i$ , so that we only need to consider the relative motion,

$$H_{rel} = \sum_{i=x,y,z} \left( \frac{\mu \omega_i^2 r_{rel,i}^2}{2} + \frac{p_{rel,i}^2}{2\mu} \right) + V_{int}(\mathbf{r}_{rel})$$

When treating the interaction as perturbation, the base solution is the harmonic oscillator states for the relative motion  $|n_{rel,x}, n_{rel,y}, n_{rel,z}\rangle$ . The energy level perturbation is then,

$$\begin{aligned} \Delta_{n_{rel,x}, n_{rel,y}, n_{rel,z}} &= \langle n_{rel,x}, n_{rel,y}, n_{rel,z} | V_{int}(\mathbf{r}_{rel}) | n_{rel,x}, n_{rel,y}, n_{rel,z} \rangle \\ &= \frac{2\pi\hbar^2 a}{\mu} \langle n_{rel,x}, n_{rel,y}, n_{rel,z} | \delta_{reg}(\mathbf{r}_{rel}) | n_{rel,x}, n_{rel,y}, n_{rel,z} \rangle \\ &= \frac{2\pi\hbar^2 a}{\mu} \left| \psi_{n_{rel,x}, n_{rel,y}, n_{rel,z}}(0) \right|^2 \end{aligned} \quad (4.1)$$

where  $\left| \psi_{n_{rel,x}, n_{rel,y}, n_{rel,z}}(0) \right|^2$  is the probability density for zero distance between the atoms.

For the motional ground state, the shift is,

$$\Delta_{0,0,0} = a \frac{2\hbar^2}{\mu\sqrt{\pi}} \prod_{i=x,y,z} \frac{1}{\beta_{rel,i}}$$

where  $\beta_{rel,i} \equiv \sqrt{\hbar/\mu\omega_{rel,i}}$  is the relative motion oscillator length along the  $i$ -th axis. The shift is proportional to the strength of the interaction  $a$ , and is also stronger for stronger confinement where the wavefunction density is higher.

We can see from (4.1) that the shift is only non-zero when all of  $n_{rel,i}$ 's are even. The shift is also smaller for higher motional excited state with smaller wavefunction density. This means that the shift will only be observable if the atom is cooled to closed to the motional ground state and will be small or zero for hot atoms.

#### 4.2.2 NON-PERTURBATIVE CALCULATION

The first order perturbative result breaks down for large  $a$  when the energy shift approaches the motional energy scale  $\omega_{rel,i}$ . Moreover, due to the divergence nature of the delta-function in the contact interaction potential, higher order perturbative calculation does not converge. It is therefore necessary to use a non-perturbative solution of the interacting atoms in order to interpret measurement of the shift for strong interaction.

(Exact solution for anisotropic trap) (Correction on top of exact solution)

### 4.3 INTERACTION SHIFT SPECTROSCOPY

(Sequence) (Result) (motional sideband, scattering length result)

### 4.4 SUMMARY AND OUTLOOK

(Motional state selection)

# 5

## Photoassociation of Single Atoms

### 5.1 INTRODUCTION

The method we use to coherently create a single molecule from atoms uses two photon optical transition<sup>(7)</sup>. Before we can drive such a transition, however, we must locate and characterize the intermediate excited states of the molecule to be used in the two-photon transition. This can be measured using photoassociation (PA) spectroscopy where two atoms are driven from the atomic

state to an excited molecular state via an optical transition. The flexibility of the optical tweezer platform allows us to prepare a clean initial state with only two atoms as well as accurately detect when PA has happened with high signal to noise ratio (5.3.2).

In this chapter, we describe the molecular energy structure (section 5.2) and how we use PA spectroscopy to locate and identify the molecular excited states (section 6.2). We also details the beam-path for the measurement (5.3.1) including the alignment procedure for the PA beam and discussions about factors that can affect the PA linewidth (5.3.3).

## 5.2 ENERGY LEVELS

First we will discuss the energy levels in a diatomic molecule as well as the labeling system for the states. We will focus mainly on the electronic excited states measured in this chapter but most of the discussion here applies to ground electronic states as well and will be useful for chapter and .

### 5.2.1 ANGULAR MOMENTUMS

Compared to an atom, a diatomic molecule has many more degrees of freedoms. In addition to the quantum numbers for each atom in the molecule, molecules also have nuclear motion. In order to reduce the complexity, it is therefore very important to consider the symmetry of the system, and in particular the angular momentums, which corresponds to rotation symmetry, and the coupling between them. The angular momentums in a diatomic molecule includes electron orbit  $\mathbf{L}^*$ ,

---

\*There are  $\mathbf{L}_1$  and  $\mathbf{L}_2$  for the two electron but since we only consider states with at most one  $\mathbf{L}_i \neq 0$  we will only use one quantum number here



**Figure 5.1:** Angular momentum coupling for *Hund's case (a)*.  $\mathbf{L}$  and  $\mathbf{S}$  are coupled to the internuclear axis  $\hat{n}$  and the sum of the projections  $\Omega = \Lambda + \Sigma$  is then added with the orthogonal component  $\mathbf{N}$  to form  $\mathbf{J}$ .

electron spin  $\mathbf{S}_1$  and  $\mathbf{S}_2$ , nuclear orbital  $\mathbf{N}$  and nuclear spin  $\mathbf{I}_1$  and  $\mathbf{I}_2$ . Although the total angular momentum  $\mathbf{F} \equiv \mathbf{L} + \mathbf{S}_1 + \mathbf{S}_2 + \mathbf{N} + \mathbf{I}_1 + \mathbf{I}_2$  is the only true conserved quantity in the absence of external field, depending on the coupling strengths between the angular momentums, there are additional approximately conserved quantity in the molecule.

For the NaCs molecule and our experiment, there are two important regimes where the coupling strength can be easily ordered.

## DEEPLY BOUND STATES

This is described by the *Hund's case (a)*. Molecular states with large binding energies mostly experience interactions between the atoms at short range where the electric static interaction is very strong. This couples the the two electron spins into a total electron spin  $\mathbf{S} \equiv \mathbf{S}_1 + \mathbf{S}_2$  via a very strong ef-

fective interaction of the form  $\mathbf{S}_1 \cdot \mathbf{S}_2$  which originates from the resulting symmetry of the electron orbital wavefunction. Similar to atoms, the nuclear spin interaction is also very weak compared to other energy scales so we can ignore the hyperfine structure and only need to consider  $\mathbf{J} \equiv \mathbf{L} + \mathbf{S} + \mathbf{N}$ .

The strong electrostatic interaction also creates an effective coupling between the  $\mathbf{L}$  and  $\mathbf{S}$  with the internuclear axis  $\hat{n}$  causing  $\mathbf{L}$  and  $\mathbf{S}$  to precess rapidly around  $\hat{n}$ . This creates two new conserved quantities  $\Lambda$  and  $\Sigma$  as the projection of  $\mathbf{L}$  and  $\mathbf{S}$  along  $\hat{n}$  respectively. The total angular momentum along  $\hat{n}$  is therefore  $\Omega \equiv \Lambda + \Sigma$  and it is added to the  $\mathbf{N}$  which is orthogonal to  $\hat{n}$  to form the total angular momentum  $\mathbf{J}$  (Fig. 5.1).

The angular momentum state of the molecule is therefore fully characterized by  $|L, \Lambda, S, \Omega, J\rangle$ .  $\Lambda$  can be  $0, 1, \dots, L$ ,  $\Omega$  ranges from  $|\Lambda - S|$  to  $\Lambda + S$  and  $J \geq \Omega$ . The  $L$  quantum number is specified by the electronic state and will be discussed in section 5.2.2 and the rest of the angular momentum quantum numbers are represented by the *Hund's case (a)* term symbol,

$$^{2S+1}\Lambda_{\Omega}$$

similar to the atomic term symbol  $^{2S+1}L_J$ . Just as the use of capital English letters  $S, P, D, \dots$  to represent  $L = 0, 1, 2, \dots$ , capital Greek letters  $\Sigma, \Pi, \Delta, \dots$  are used to denote  $\Lambda = 0, 1, 2, \dots$  in the term symbol. An additional symmetry to consider is the reflection about a plane that includes the internuclear axis. For  $\Lambda > 0$  states, the reflection produces a new state at the same energy creating the so-called  $\Lambda$ -doubling. For  $\Lambda = 0$  states, i.e.  $\Sigma$  states, the reflection produces the same state with a phase of  $\pm 1$ . This phase is also included in the term symbol to fully specify the symmetry of a  $\Sigma$



states as

$$^{2S+1}\Sigma_{\Omega}^{\pm}$$

Note the  $\Sigma$  state here should not be confused with the quantum number  $\Sigma$ .

From the angular momentum relation in Fig. 5.1, we can also determine the energies of different rotational states. The nuclear rotational energy is given by,

$$E_{rot} = B\langle \mathbf{N}^2 \rangle$$

where  $B$  is the rotational constant of the molecule. For *Hund's case (a)* this is,

$$\begin{aligned} E_{rot} &= B\langle \mathbf{J}^2 - \Omega^2 \rangle \\ &= B\langle \mathbf{J}^2 - \Omega^2 \rangle \\ &= B(J(J+1) - \Omega^2) \end{aligned}$$

For the last step, note that  $\Omega$  is not an angular momentum vector but a projection. We can easily see that for a given  $\Omega$ , we have  $J \geq \Omega$ . Unlike a rigid rotor where  $E_{rot} = BN(N+1)$ , the limit on the  $J$  means that the spacing between the rotational levels depend on  $\Omega$ ,

$$2\Omega + 2, 2\Omega + 4, 2\Omega + 6, \dots$$

This allows us to determine the  $\Omega$  of the state we are addressing by measuring the state spacing for

the lowest few rotational states.

## NEAR THRESHOLD BOUND STATES

For molecular states with small binding energy, the interaction between the two atoms is small compared to the internal coupling in the atoms and the angular momentum coupling is “atom like”. In this limit, the total angular momentum  $\mathbf{F}_1$  and  $\mathbf{F}_2$  for the individual atoms forms  $\mathbf{F}_{atom} = \mathbf{F}_1 + \mathbf{F}_2$  which is then coupled to the nuclear rotation  $\mathbf{N}$  to form  $\mathbf{F} = \mathbf{F}_{atom} + \mathbf{N}$ . We will discuss this regime in more detail when we characterize the weakly bound ground states in chapter 6.

### 5.2.2 POTENTIAL ENERGY SURFACE

Due to the different angular momentum coupling in different regimes, there is not a consistent way to label the interaction between the two atoms at both short and long distance. Nevertheless, by convention, we use the *Hund’s case (a)* term symbol since it more accurately represents the state when the interaction energy dominates.

The Hamiltonian (excluding spin for simplicity<sup>†</sup>) is,

$$H = H_e + T_n$$

---

<sup>†</sup>Electron spin is implicitly included, however, via the symmetry of the electronic wavefunction.

where the electronic term  $H_e$  and the nuclear kinetic term  $T_n$  are given by

$$H_e = - \sum_i \frac{\hbar^2}{2m_e} \nabla_i^2 + \frac{e^2}{4\pi\epsilon_0} \left( \sum_{i>j} \frac{1}{|\mathbf{r}_i - \mathbf{r}_j|} - \sum_{A=Na,Cs} \sum_i \frac{Z_A}{|\mathbf{r}_i - \mathbf{R}_A|} + \frac{Z_{Na}Z_{Cs}}{|\mathbf{R}_{Cs} - \mathbf{R}_{Na}|} \right) \quad (5.1)$$

$$T_n = - \sum_{A=Na,Cs} \frac{\hbar^2}{2m_A} \nabla_A^2$$

and the sum is over all the electrons in the molecule.

## BORN-OPPENHEIMER APPROXIMATION

The Hamiltonian is solved using the Born-Oppenheimer (BO) approximation. Because of the large mass difference between the nuclei and the electrons, we can assume that the electron motion follows the position of the nuclei instantaneously so that the motion of the nuclei and the electrons can be treated separately. Formally, this means that the electron wavefunctions are solved using the electronic term  $H_e$  for a given nuclear position  $\mathbf{R}_{Na}$  and  $\mathbf{R}_{Cs}$ . This results in an effective potential  $V_{eff}(|\mathbf{R}_{Na} - \mathbf{R}_{Cs}|)$  called the potential energy surfaces (PES) for each electronic state. The solutions to the approximate Hamiltonians  $T_n + V_{eff}$  provide the vibrational and rotational states of the molecule.

## FRANCK-CONDON FACTOR

In addition to the energy of the molecular bound state, the solution of the nuclear motion also provides information to the selection rules and coupling strength of transitions between the states. For an electronic electric dipole transition between state  $|e_1, v_1, j_1\rangle$  and  $|e_2, v_2, j_2\rangle$ , where  $e_i, v_i$  and

$j_i$  denotes electronic, vibrational and angular momentum states, the Rabi frequency under the BO approximation is,

$$\begin{aligned}\Omega &= \langle e_1, v_1, j_1 | e \mathbf{r}_e \cdot \mathbf{E} e^{i\mathbf{k} \cdot \mathbf{r}} | e_2, v_2, j_2 \rangle \\ &= \langle e_1(\mathbf{r}) | e \mathbf{r}_e \cdot \mathbf{E} | e_2(\mathbf{r}) \rangle \langle v_1, j_1 | e^{i\mathbf{k} \cdot \mathbf{r}} | v_2, j_2 \rangle\end{aligned}$$

where  $\mathbf{r}$  and  $\mathbf{r}_e$  are the molecule and electron coordinates. For most of the transitions, we can treat the nuclear coordinate dependent transition dipole moment  $\mathbf{D}(\mathbf{r}) \equiv \langle e_1(\mathbf{r}) | e \mathbf{r}_e | e_2(\mathbf{r}) \rangle$  as a constant  $\mathbf{D}$ . Since the size of the molecular wavefunction is also usually much smaller than the wavelength of the transition, we can also assume  $e^{i\mathbf{k} \cdot \mathbf{r}} \approx 1$ , we have,

$$\Omega = \mathbf{D} \cdot \mathbf{E} \langle j_1 | j_2 \rangle \langle v_1 | v_2 \rangle$$

The term  $\langle j_1 | j_2 \rangle$  determines the angular momentum selection rule which is  $\Delta \Lambda = 0, \pm 1$ ,  $\Delta S = 0$ ,  $\Delta \Sigma = 0, \pm 1$  and  $\Delta J = 0, \pm 1$  for *Hund's case (a)*<sup>Straughan</sup>. The term  $\langle v_1 | v_2 \rangle$  gives the coupling strength between vibrational states<sup>‡</sup>. This is called the Franck-Condon principle and the square of the wavefunction overlap is defined as the Franck-Condon factor (FCF),

$$\text{FCF} \equiv |\langle v_1 | v_2 \rangle|^2$$

---

<sup>‡</sup>Note that  $\langle v_1 | v_2 \rangle$  does not simplify to orthogonality relation when  $e_1 \neq e_2$  since the vibrational wavefunctions belongs to different PES.

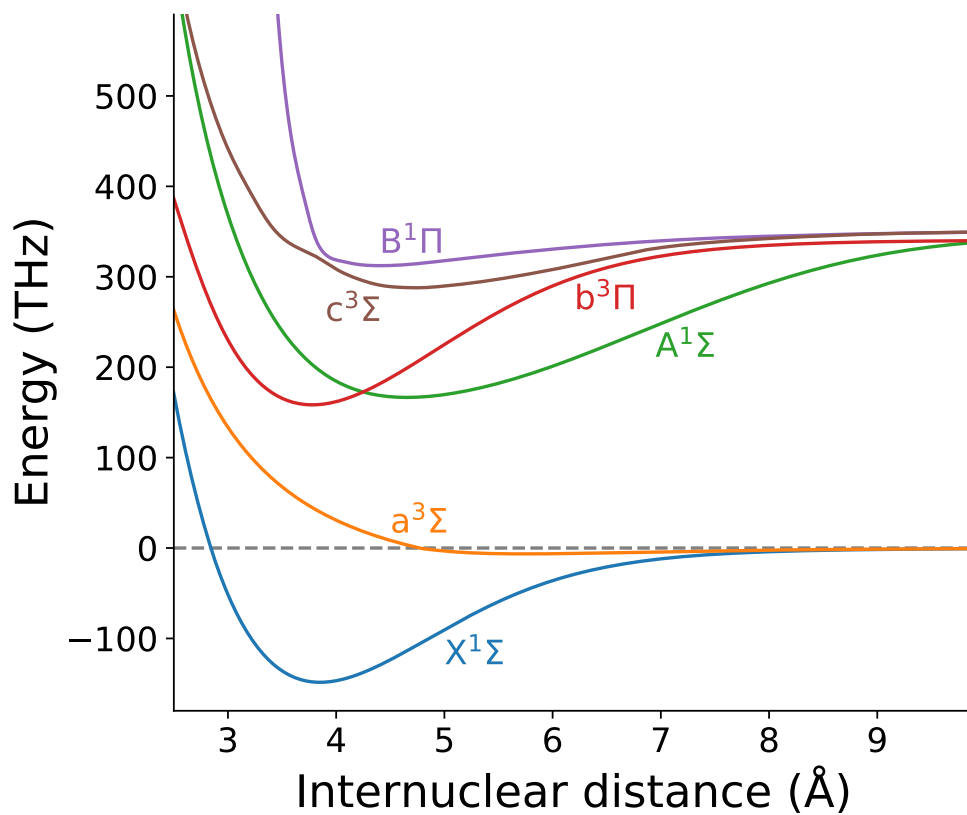


**Figure 5.2:** Potential energy surfaces of NaCs with *Hund's case (a)* labels. Due to spin-orbit coupling, the potentials are not independent of each other. The real energy eigenstates of the molecule may be a superposition of multiple electronic and spin states.

For incoherent transition, the transition rate is proportional to  $\Omega^2 \propto \text{FCF}$ .

#### ENERGY LEVEL OF NaCs

Fig. 5.2 shows the relevant PESs for NaCs. Although the spin-less electronic Hamiltonian 5.1 makes it easier to understand the molecule structure and provides good approximations for the transition dipoment and FCF, the absense of spin and the difficulty in exactly solving a multi-electron system makes it unsuitable to calculate energy levels for spectroscopy purpose. Because

of this, prediction of the molecular states energies are calculated using PESs fitted to experimental data <sup>Docenko et al., Zaharova et al., 3, 2</sup>.

### 5.3 PHOTOASSOCIATION SPECTROSCOPY

#### 5.3.1 BEAMPATH

The excited molecular state we would like to address has a bond length of 3 – 8. The initial atomic state, however, has an average inter-nuclear distance of  $\approx 1000$ . This size mismatch between the initial and final state wavefunctions means the transition typically have a very small FCF ( $10^{-10}$  –  $10^{-8}$ ). Because of this, we focus our PA beam onto the tweezer with a beam waist between  $10\mu\text{m}$  and  $30\mu\text{m}$  (Fig. 5.3) in order to increase the laser intensity and improve the signal contrast. The tight focus also increase the astigmatism when passing through the glass cell window at an angle which limits the minimum focus size we can achieve. Therefore, we added a correction glass plate to fix the astigmatism in order to minimize the focus size and maximize the beam intensity.

In order to align the PA beam to the tweezer, we use the following alignment procedure,

1. Light resonant with the Cs atomic transition is sent into the PA beam path. This allows us to do the alignment using the procedure we used to align the atomic Raman sideband cooling beams as described in section 3.8. However, unlike the alignment for the atomic Raman beams, due to the larger frequency difference between the PA transition and the Cs atomic transition as well as the smaller beams size, we cannot use the alignment result from this step directly for the PA beam due to the chromatic aberration from the optics in the PA beam path.
2. In order to translate the alignment result from resonance Cs light to that of the PA light, we insert a mirror to reflect the PA beam after the last optics in the beam path and place a beam profiler at the equivalent location of the tweezer (Fig. 5.3). This allow us to directly measure



**Figure 5.3:** PA beampath including the relative geometry with the magnetic field the glass vacuum cell and the tweezer. In order to compensate for the astigmatism from pass through the glass cell window at an angle, we added an correction glass plate into the PA beam path. The correction plate has the same thickness and angle of incident with the glass cell window but is angled vertically instead of horizontally. The alignment mirror and the beam profiler can also be added to the beam path in order to measure the chromatic error during alignment.



**Figure 5.4:** Measurement of Cs vector light shift from the PA beam for final alignment. (A) The effective magnetic field from the circularly polarized PA beam causes a shift on the Raman resonance between the  $|4, 4\rangle$  and  $|3, 3\rangle$  states. (B) Vector light shift as a function of PA beam position used to determine the beam center. The  $1/e$  diameter of the beam is measured to be  $13.40(72)\mu\text{m}$ .

location of the focal point for the two wavelengths and correct for the chromatic aberration by shifting the focus from the PA light to the original focus position from the resonance Cs light.

3. As the final alignment step and to correct for the chromatic aberration of the glass window that was not corrected for in the last step, we align the PA beam to the atom using signal directly from the atom. Due to the large detuning, the scattering rate from the PA beams is too low to be used for alignment. However, when the PA beam is set to circular polarization, it creates an effective magnetic field parallel to the beam propagation direction of the form <sup>Thompson et al.</sup>,

$$B_{\text{eff}} = -U_0 \frac{\delta_2 - \delta_1}{\delta_2 + 2\delta_1} \mathbf{C}$$

where  $U_0$  is the scalar light shift,  $\delta_1$  and  $\delta_2$  are the detuning from the  $D_1$  and  $D_2$  line respectively,  $\varepsilon$  is the polarization vector and  $\mathbf{C} \equiv \Im(\varepsilon \times \varepsilon^*)$  qualifies the ellipticity of the polarization with  $|\mathbf{C}| = 1$  for pure circular polarization and  $|\mathbf{C}| = 0$  for linear polarization. This effective magnetic field causes a relative shift between the  $|4, 4\rangle$  and the  $|3, 3\rangle$  states which can be measured using a Raman transition (Fig. 5.4A). By measuring the shift as a function of the beam position, we can determine the size and the center of the PA beam and align the beam to the atom (Fig. 5.4B).



### 5.3.2 EXPERIMENT SEQUENCE AND RESONANCE FREQUENCIES

For the PA spectroscopy, we mainly focus on states with large binding energies which are expected to be good candidates as the intermediate state for Raman transfer<sup>(7,2)</sup>. In particular, we scanned the PA light frequency around the  $v' = 0$  and  $v' = 12 - 14$  vibrational states in the  $c^3\Sigma$  potential.

In order to observe PA, we first prepare both the Na and Cs atoms in the motional ground states in the same tweezer [Liu et al.](#). We then turn on the PA beam to a set power for a set time followed by separating the atoms into their respective tweezers and image the atoms. When we hit a PA resonance, the excited molecular state will typically decay down to either a molecular ground state, which will remain in at most one of the tweezers after the separation, or an atomic state with high relative motional energy and escape the trap. In either case, this leads to at least one empty tweezer after the separation. By measuring the probability of having both the Na and Cs atoms after the PA pulse conditioned on both atoms being initially loaded, we can capture the probability of PA event and locate the resonances.

### 5.3.3 LINEWIDTH

In addition to the energy, another property of the excited state that is important for driving a two-photon transition using the state is the linewidth. This determines the scattering or decoherence rate of the two-photon transition which then determines the transfer efficiency<sup>(7)</sup>.

# 6

## Two-photon Spectroscopy of NaCs

### Ground State

#### 6.1 INTRODUCTION

The excited molecular states measured and characterized in chapter 5 provide us a pathway to couple to the ground electronic molecular states using two-photon transitions. While it is in principle

possible to drive from the atomic state to any desired molecular ground state for various applications, doing so directly has many technical challenges. We will cover these challenges as well as the considerations in selecting the molecule formation pathway in chapter 7, however, the difficulty, and the main difference from a pure atomic Raman transition, lies in the wavefunction size mismatch. As we have seen already in section 5.3.1, the size mismatch between the excited molecular states and the ground atomic state causes a very small FCF and requires a high PA intensity to improve the signal strength. This small FCF also reduces the Rabi frequency for the two-photon transition to the ground state. As a result, driving a two-photon transition to an arbitrary molecular ground state may require maintaining coherence between two different lasers over a relatively long time (milliseconds) which is very difficult to achieve.

Our solution to this challenge is to do the transfer via a two step process.

1. We drive a two-photon transition from the atomic state to a weakly bound ground state. The reduced energy difference allows the laser coherence to be maintained over a longer time easily. In the case of NaCs molecule, this also increases the FCF between the ground and excited molecular states which allows shorter pulse time and further reduces the coherence requirement.
2. The transfer to arbitrary molecular ground state will be done from the weakly bound state created in the first step. The strength of this transition can be much higher and only requires a relatively shorter laser coherence time. This step has already been demonstrated in other experiments so in this thesis we will focus only on the first step transfer.

In this chapter, we will discuss the use of Raman spectroscopy to measure the properties of the weakly bound molecular ground states. In section 6.2 we will describe the states involved and the setup for the Raman spectroscopy as well as the measured binding energy for the  $N = 0$  states. In

section 6.3 we study the coupling between angular momentums for near threshold molecular states by characterizing the  $N = 2$  states.

## 6.2 WEAKLY BOUND NACs GROUND STATES

As mentioned in section 5.2.1, the angular momentum coupling for weakly bound molecular state is similar to that of the atoms. Therefore, instead of using the term symbol for the *Hund's case (a)* to identify the molecular potential and bound states, we use the hyperfine state ( $F_{Na}, F_{Cs}$ ) for the atoms instead.

In order to measure the binding energy of a molecular state, we first prepare the atom in the corresponding hyperfine state and drive a Raman transition to the molecular state. We use a Raman transition that is detuned from the  $c^3\Sigma v' = 0$  state measured in section . When the Na and Cs are in the same tweezer, they can undergo fast spin-exchange collision that changes the hyperfine state of the atom. This process can cause the hyperfine energy ( $> 1\text{GHz}$ ) of the atoms to be transferred to the motional energy and eject the atoms from the tweezer ( $< 100\text{MHz}$  deep). As a result, the measurement can only be done when the spin-exchange collision is suppressed, which includes the following spin combinations,

1.  $F_{Na} = 1$  and  $F_{Cs} = 3$

This is the spin state with the lowest energy and therefore the spin-exchange interaction is energetically forbidden. In the experiment, we use the state  $|Na(1, 1), Cs(3, 3)\rangle$  which can be prepared from the  $|Na(2, 2), Cs(4, 4)\rangle$  state from OP easily by driving a Raman transition for both Na and Cs atoms. This state also remains the lowest energy atomic state in the present of a weak magnetic field.

2.  $|Na(2, 2), Cs(4, 4)\rangle$  and  $|Na(2, 2), Cs(3, 3)\rangle$  \*

These spin states are stable because the spin-exchange collision conserves total  $m_F$  of the two atoms and the two states are the lowest energy states that has the same total  $m_F$ . Inelastic collision that changes the total  $m_F$  can also happen but has a lower collision rate since it requires transferring angular momentum between the spin and motion of the atom.

### 6.2.1 DRIVING RAMAN TRANSITION USING THE OPTICAL TWEEZER

In order to increase the intensity of the Raman beams to overcome the small FCF, we use the tweezer beam to drive the Raman transition. Not only does this maximizes the intensity due to the small focal size of the tweezer, since the atoms are trapped at the maximum of the tweezer beam, this also ensures that the Raman beam is aligned automatically to the atoms and suppresses sensitivity to mechanical fluctuation that is usually caused by a small beam size. Moreover, this also minimizes the number of beams the atoms experience during the Raman transition which, in turns, minimizes the scattering. As a result, the coherence of the transition is also improved which is important for achieving coherent creation of molecule (chapter 7).

The beampath to generate the required frequencies in the tweezer is shown in Fig. 6.1. Care must be taken to avoid interference of beam causing power fluctuation.

### 6.2.2 RAMAN RESONANCE ON $v'' = -1$ , $N = 0$ GROUND STATE

## 6.3 ANGULAR MOMENTUM COUPLING IN $N = 2$ GROUND STATE

---

\*States with opposite  $m_F$ , i.e.  $|Na(2, -2), Cs(4, -4)\rangle$  and  $|Na(2, -2), Cs(3, -3)\rangle$  are also stable but are omitted here since these cannot be easily prepared in our experiment.

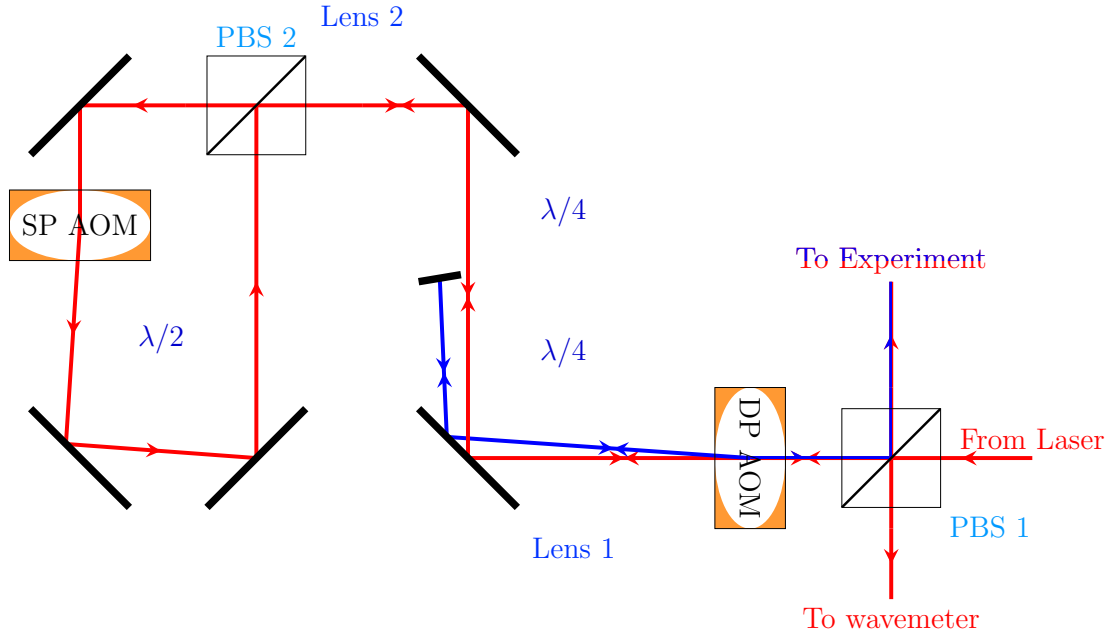


**Figure 6.1:** Beampath for generating the frequency for Raman transition in the tweezer. (Beampath for fiber coupling and overall power control is not shown.) The red beam path is the 0-th order of the double pass (DP) AOM which is used for the tweezer. When the DP AOM is turned on, some power is redirected to the first order (blue beam path) which generates the required frequency different to drive the Raman transition. The two frequencies are recombined on the DP AOM. The 0-th order light is shifted by another single pass (SP) AOM running on a different frequency before recombining. Without this AOM, the leak light from the DP AOM will be at the same frequency as the 0-th order light which can cause a significant power fluctuation due to interference. The SP AOM ensures that none of the leaking light frequency coincide with either intended frequencies therefore avoiding this issue. Different selection of the SP and DP AOM as well as their orders can be used to cover a wide range of two photon detuning for Raman transition. The experiment typically start with the SP AOM on and the DP AOM off. When driving the Raman transition, the powers on both AOMs are ramped simultaneously to achieve the desired power at both frequencies.

7

# Coherent Optical Creation of NaCs

## Molecule

### 7.1 INTRODUCTION

### 7.2 RAMAN TRANSITION BEYOND THREE-LEVEL MODEL

For a Raman transition with Raman Rabi frequency  $\Omega_R$  and total scattering rate  $\Gamma$ , defined as the sum of the scattering rate for the initial and final states, the probability of scattering during a  $\pi$  pulse is,

$$\begin{aligned} p_{scatter} &= \frac{\Gamma t_\pi}{2} \\ &= \frac{\pi\Gamma}{2\Omega_R} \end{aligned}$$

which is proportional to the ratio  $\Gamma/\Omega_R$ . In an ideal three-level system, this is the only source of decoherence which can be made arbitrarily small by using a large single photon detuning<sup>(3.2.1)</sup>. However, in a real system, there are often other effects that increases the scattering and may also put a lower limit on the scattering probability during the transfer. Fig. 7.1 shows a generic model for a real Raman transition demonstrating some of these effects. Additionally, other practical limitation in the





**Figure 7.1:** Generic model for a real Raman transition. The initial state  $|i\rangle$  and the final state  $|f\rangle$  has a energy difference  $\delta$  and are coupled by two Raman beams with frequencies and single photon Rabi frequencies of  $\nu_1, \Omega_1$  and  $\nu_2, \Omega_2$  respectively. The corresponding matrix elements (arbitrary unit) are  $M_1$  and  $M_2$ . The Raman beams are detuned by  $\Delta$  from the primary excited state  $|e\rangle$ , which has a decay rate of  $\Gamma_e$ . We also consider additional states near the initial ( $|i'\rangle$ ), final ( $|f'\rangle$ ) and intermediate excited  $|e'\rangle$  states which are separated from the corresponding Raman transition states by  $\omega'_i, \omega'_f$  and  $\omega'_e$  respectively. Only one additional state of each kinds are included to simplify the discussion without loss of generality.

system like stability of the laser power and frequency also needs to be taken into account.

In the experiment, we find the parameter range that gives the best transfer efficiency using numerical simulation (see section 7.4). Nevertheless, in order to develop a general approach that can be applied to other systems, it is also important to understand the various physical mechanism that leads to the optimal parameters. Therefore, in this section, we will discuss some of the most important effects on the transfer efficiency at qualitative and semiquantitative level. Due to experimental

constraint, we will assume that the single photon detuning is much smaller than the frequency of each individual beams, i.e.  $\Delta \ll \nu_1, \nu_2$ .

### 7.2.1 ADDITIONAL INITIAL AND FINAL STATES

First, we will discuss the effect of  $|i'\rangle$  and  $|f'\rangle$  states near the initial and final states. These states can be coupled to the excited state  $|e\rangle$  by the Raman beams, which can in turn be coupled to the initial and final states by an off-resonance Raman transition. The leakage is suppressed by the detuning from the Raman resonance, i.e.  $\omega'_i$  and  $\omega'_f$ . This puts a limit on the Raman Rabi frequency  $\Omega_R$  to be smaller than the smallest energy gap, which in turn puts a limit on the minimum Raman transfer time. In our experiment, the minimum energy gap comes from axial motional excitation of the atomic initial states which is between  $2\pi \times 10 - 30$  kHz depending on the trap depth used. The typical Raman  $\pi$  time we can realize is  $0.5 - 5$  ms so this effect is not a major limiting factor for our transfer efficiency.

### 7.2.2 ADDITIONAL EXCITED STATES

Next, we will consider the effect of the  $|e'\rangle$  state near the excited intermediate state. These states can be coupled to the ground states, both  $|i\rangle$  and  $|f\rangle$ , by the Raman beams and can cause a change in both the Raman Rabi frequency and the scattering rate. The total Raman Rabi frequency (Fig. 7.2A) is,

$$\Omega_{Raman} = \frac{\Omega_1 \Omega_2}{2\Delta} + \frac{\Omega'_1 \Omega'_2}{2(\Delta - \omega'_e)}$$

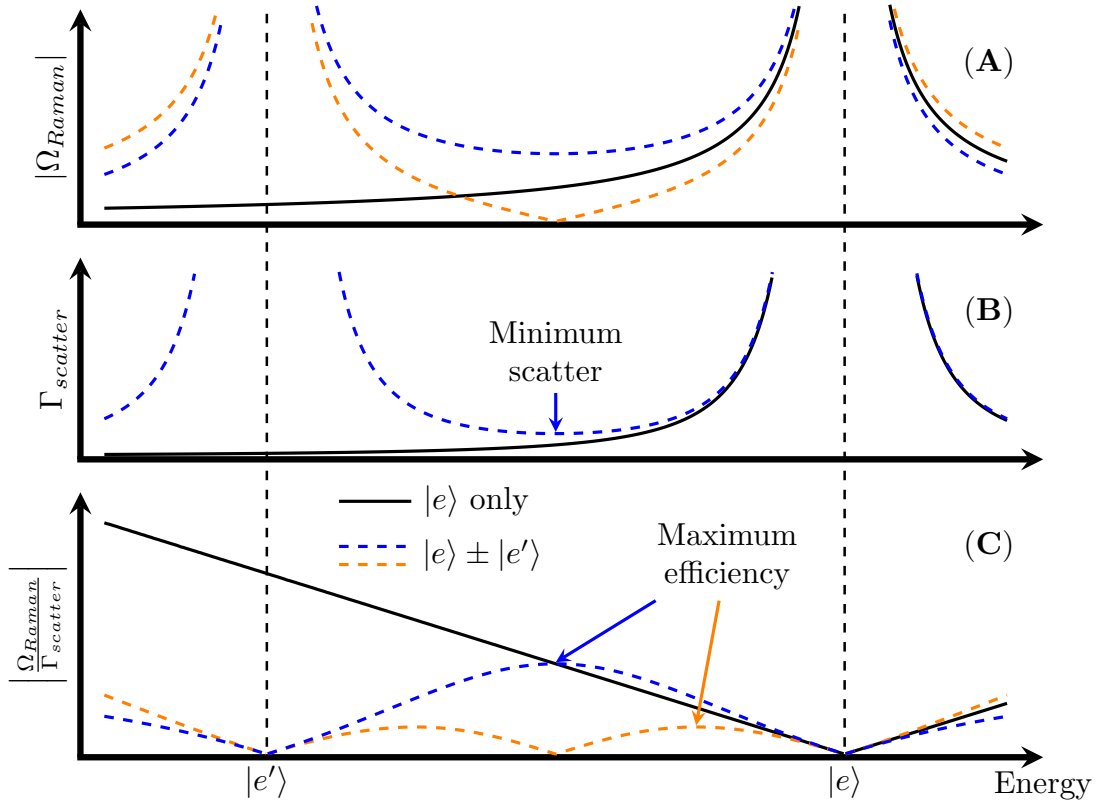


**Figure 7.2:** Effect of additional excited states  $|e'\rangle$  on the Raman transition efficiency. (A) Depending on the sign of the coupling, there could be constructive (blue) or destructive (orange) interference on the Raman Rabi frequency  $\Omega_{Raman}$ . (B) Increased scattering rate  $\Gamma_{scatter}$  caused by  $|e'\rangle$  with a minimal between the two states. (C) Optimal detunine exists between the two states with maximum transfer efficiency corresponds to a fraction of the state spacing.

where  $\Omega'_1$  and  $\Omega'_2$  are the single photon Rabi frequencies coupling  $|e'\rangle$  to  $|i\rangle$  and  $|f\rangle$  respectively. Depending on whether  $\Omega'_1\Omega'_2$  has the same (orange line) or different (blue line) sign as  $\Omega_1\Omega_2$ , the total Raman Rabi frequency may be cancelled or enhanced between the two excited states. On the other hand, the total scattering rate (Fig. 7.2B) is almost always increased due to the additional state, creating a local minimum between the excited states. Combining the two effects, the ratio between the Raman Rabi frequency and the scattering rate, which determines the transfer efficiency, always have local maximum between the excited states (Fig. 7.2C).

Despite the difference in the position and value of the maximum for different  $|e'\rangle$  parameters, we can summarize the effect on the transfer efficiency as a limit on the maximum detuning  $\Delta_{max}$  to a fraction of the spacing between the excited states ( $\omega'_e$ ). As an example, the blue and orange maxima in Fig. 7.2C corresponds to a limit on single photon detuning of  $0.5\omega'_e$  and  $0.15\omega'_e$ . As one would expected, a larger excited state spacing usually result in a larger detuning limit and a better transfer efficiency.

Summarizing the effect of additional excited state as a single number  $\Delta_{max}$  allows us to keep using the equation for Raman transition with minor corrections and makes it easier to compare different state selection and transition schemes. It is also worth noting that although only one additional excited state  $|e'\rangle$  is considered here, this result can be generalized when more excited states are taken into account as well. These states introduces additional smooth variation in both the Raman Rabi frequency and scattering rate and the effects on the final transition efficiency can be similarly treated as a change in the maximum detuning.

### 7.2.3 CROSS COUPLING BETWEEN LIGHT ADDRESSING INITIAL AND FINAL STATES

Due to the small energy separation between the initial and final state  $\delta$ , the cross coupling of the laser addressing the initial/final state on the final/initial state is another important effect in our experiment. Without the cross coupling, the total off resonance scattering rate for the initial and the final states is

$$\Gamma_{scatter0} = \frac{\Gamma_e (\Omega_1^2 + \Omega_2^2)}{4\Delta^2}$$

For a given Raman Rabi frequency  $\Omega_{Raman} \propto \Omega_1 \Omega_2$ , this is minimized when  $\Omega_1 = \Omega_2$ .

When cross coupling is taken into account, however, the total scattering rate becomes, \*

$$\Gamma_{scatter} = \frac{\Gamma_e \Omega_1^2}{4M_1^2} \left( \frac{M_1^2}{\Delta^2} + \frac{M_2^2}{(\Delta + \delta)^2} \right) + \frac{\Gamma_e \Omega_2^2}{4M_2^2} \left( \frac{M_2^2}{\Delta^2} + \frac{M_1^2}{(\Delta - \delta)^2} \right) \quad (7.1)$$

$$\propto \frac{\Gamma_e P_1}{4} \left( \frac{M_1^2}{\Delta^2} + \frac{M_2^2}{(\Delta + \delta)^2} \right) + \frac{\Gamma_e P_2}{4} \left( \frac{M_2^2}{\Delta^2} + \frac{M_1^2}{(\Delta - \delta)^2} \right) \quad (7.2)$$

where  $P_{1,2} \propto \Omega_{1,2}^2/M_{1,2}^2$  are the powers of the laser beams 1 and 2. When  $\delta \ll \Delta$  such as our experiment,

$$\begin{aligned} \Gamma_{scatter} &\approx \frac{\Gamma_e (M_1^2 + M_2^2)}{4\Delta^2} \left( \frac{\Omega_1^2}{M_1^2} + \frac{\Omega_2^2}{M_2^2} \right) \\ &\propto \frac{\Gamma_e (M_1^2 + M_2^2)}{4\Delta^2} (P_1 + P_2) \end{aligned}$$

---

\*Here we assume that the matrix elements are the same for the two beams. This is the case when the two beams have the same polarization as in our experiment. This effect can be minimized or eliminated by selecting different polarizations for the two laser frequencies that does not couple to the other initial/final state. This would also require choosing an excited state with the same or lower angular momentum as the ground states in order to avoid cross coupling to different excited states.

For a given Raman Rabi frequency  $\Omega_{Raman} \propto \Omega_1 \Omega_2 \propto \sqrt{P_1 P_2}$ , this is minimized when  $P_1 = P_2$ . Hence, due to the strong cross coupling, we need to use the same power in both Raman beams rather than adjusting the powers to match their single photon Rabi frequencies.

Moreover, at the minimum scattering rate, we have  $\Omega_2 = \Omega_1 M_2 / M_1$  and the ratio between Raman Rabi frequency and scattering rate is,

$$\begin{aligned} \frac{\Omega_{Raman}}{\Gamma_{scatter}} &= \frac{\Omega_1 \Omega_2}{2\Delta} \frac{4\Delta^2}{\Gamma_e (M_1^2 + M_2^2)} \bigg/ \left( \frac{\Omega_1^2}{M_1^2} + \frac{\Omega_2^2}{M_2^2} \right) \\ &= \frac{2\Delta \Omega_1 \Omega_2}{\Gamma_e (M_1^2 + M_2^2)} \bigg/ \left( \frac{\Omega_1^2}{M_1^2} + \frac{\Omega_2^2}{M_2^2} \right) \\ &= \frac{\Delta \Omega_1^2 M_2}{\Gamma_e M_1 (M_1^2 + M_2^2)} \frac{M_1^2}{\Omega_1^2} \\ &= \frac{\Delta}{\Gamma_e} \frac{M_1 M_2}{M_1^2 + M_2^2} \end{aligned}$$

Therefore, for a given excited state linewidth  $\Gamma_e$  and maximum detuning (section 7.2.2) the transfer efficiency maximizes for the smallest  $M_1 M_2 / (M_1^2 + M_2^2)$  which happens when the ratio  $M_1 / M_2$  is the closest to 1.

The light shift of the Raman resonance is similarly affected by the cross coupling. The differential light shift between the initial and the final state determines the resonance fluctuation as a function of light intensity fluctuation. The ration between the light shift and the Raman Rabi frequency, i.e. line width, determines the stability requirement of our laser indensity. With cross coupling, the

differential shift is (assuming  $\delta \ll \Delta$ ),

$$\begin{aligned}\Delta\delta &\approx \frac{\Omega_1^2}{4\Delta} - \frac{\Omega_1^2 M_2^2}{4\Delta M_1^2} - \frac{\Omega_2^2}{4\Delta} + \frac{\Omega_2^2 M_1^2}{4\Delta M_2^2} \\ &= \frac{M_1^2 - M_2^2}{4\Delta} \left( \frac{\Omega_1^2}{M_1^2} + \frac{\Omega_2^2}{M_2^2} \right) \\ &\propto \frac{M_1^2 - M_2^2}{4\Delta} (P_1 + P_2)\end{aligned}$$

which is also minimized when  $P_1 = P_2$  at a given Raman Rabi frequency.

The ratio with the Raman Rabi frequency is,

$$\begin{aligned}\frac{\Delta\delta}{\Omega_{Raman}} &\approx \frac{M_1^2 - M_2^2}{4\Delta} \left( \frac{\Omega_1^2}{M_1^2} + \frac{\Omega_2^2}{M_2^2} \right) \frac{2\Delta}{\Omega_1 \Omega_2} \\ &= \frac{M_1^2 - M_2^2}{2\Omega_1 \Omega_2} \left( \frac{\Omega_1^2}{M_1^2} + \frac{\Omega_2^2}{M_2^2} \right) \\ &= \frac{M_1^2 - M_2^2}{M_1 M_2}\end{aligned}$$

the absolute value of which is also minimized when the ratio  $M_1/M_2$  is the closest to 1.

Due to the coupling strength difference, we have  $M_2 \gg M_1$  in our experiment, which means,

$$\left| \frac{\Delta\delta}{\Omega_{Raman}} \right| \approx \frac{M_2}{M_1}$$

In order to keep the resonance stable within the linewidth of the Raman resonance, i.e.  $\Omega_{Raman}$ , we need to maintain a relative stability of  $\Delta\delta$ , therefore relative stability of the laser power to better than  $M_1/M_2$ .

### 7.3 STIRAP

An alternative method often used to create and prepare the internal states of ultracold molecule is stimulated Raman adiabatic passage (STIRAP). Compared to Raman transition, which uses detuning from the excited state to reduce scattering during the transfer, STIRAP relies on a superposition between the initial and final state as a dark state to achieve the same goal. The dark state in STIRAP is created due to a destructive interference of transition from the initial and final state to the excited state.

Similar to Raman transfer, STIRAP in an ideal three-level system can achieve full coherent transfer with arbitrarily small scattering probability when given unlimited time and power budget. However, in reality, states and coupling that exist outside the ideal three-level system always cause a non-zero probability of scattering loss (see Fig. 7.3). In this section, we will apply the approach we took for Raman transition to STIRAP. We will then compare the loss caused by different practical limitations and discuss which approach should be taken under certain circumstance.

#### 7.3.1 STIRAP FOR IDEAL THREE-LEVEL SYSTEM

During STIRAP, the system approximately remains in a dark state  $|D(t)\rangle$

$$|D(t)\rangle = c_i(t)|i\rangle + c_f(t)|f\rangle$$



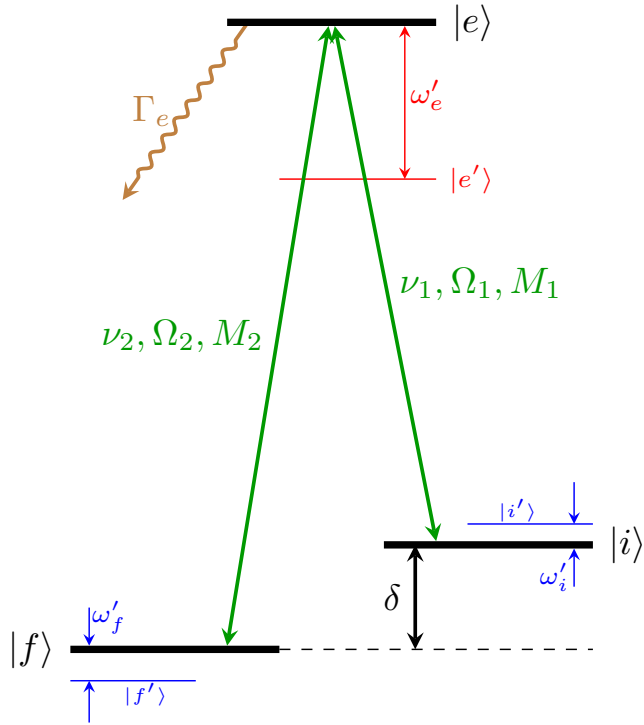


**Figure 7.3:** Generic model for a real STIRAP similar to Fig. 7.1. Differences are that the two beams are now on resonant with  $|e\rangle$  and the  $\Omega_1$  and  $\Omega_2$  now represent the maximum single photon Rabi frequency during the STIRAP pulse for the two beams.

Since this state does not couple to the excited state, we have,

$$\begin{aligned}
0 &= \langle e | \mathbf{d} \cdot \mathbf{E} | D(t) \rangle \\
&= c_i(t) \langle e | \mathbf{d} \cdot \mathbf{E} | i \rangle + c_f(t) \langle e | \mathbf{d} \cdot \mathbf{E} | f \rangle \\
&= c_i(t) \Omega_1(t) + c_f(t) \Omega_2(t)
\end{aligned}$$

or

$$|D(t)\rangle = \frac{\Omega_2(t)|i\rangle - \Omega_1(t)|f\rangle}{\sqrt{\Omega_1^2(t) + \Omega_2^2(t)}}$$

In order to estimate the scattering rate, we use the fact that the wavefunction amplitude in the final state  $c_f$  is the integral of the excited state amplitude  $c_e$  and the down leg Rabi frequency  $\Omega_2$ , i.e.,<sup>†</sup>

$$c_f(t) = \int_0^t \frac{i\Omega_2(t')}{2} c_e(t') dt'$$

For a complete transfer of length  $T$ , we have  $c_f(0) = 0$  and  $c_f(T) = 1$ , therefore,

$$\int_0^T \Omega_2(t) c_e(t) dt = -2i$$

---

<sup>†</sup>This equation and the lower bound on scattering probability applies generically to all two photon transfer process including Raman  $\pi$  pulse. The equation we used in section 7.2 is a refinement on this limit.

Since  $\Omega_2$  is the upper bound of  $|\Omega_2(t)|$  we have,

$$\left| \int_0^T c_e(t) dt \right| \geq \frac{2}{\Omega_2}$$

The total scattering probability is,

$$\begin{aligned} p_{scatter0} &= \int_0^T \Gamma_e |c_e^2(t)| dt \\ &\geq \frac{\Gamma_e}{T} \left| \int_0^T c_e(t) dt \right|^2 \\ &\geq \frac{4\Gamma_e}{\Omega_2^2 T} \end{aligned}$$

From similar argument, we also have,

$$p_{scatter0} \geq \frac{4\Gamma_e}{\Omega_1^2 T}$$

which is the same as the previous result for a three-level STIRAP system where  $\Omega_1 = \Omega_2$ . In the generic case, these give us a lower bound on the scattering probability,

$$\min(p_{scatter0}) = \frac{4\Gamma_e}{\min(\Omega_1^2, \Omega_2^2) T}$$

whereas the full scattering is larger than this lower bound by a pulse shape dependent small constant factor. It is also easy to verify that this result agrees with the scattering probability for a optimal three-level Raman  $\pi$  with similar single photon Rabi frequency and pulse time. This confirms that

without additional constraint from the real system or the experimental setup, neither Raman transfer or STIRAP offers a significant advantage over the other. As we will see in the following sections, other effects in the system can favor one approach over the other one.

### 7.3.2 ADDITIONAL INITIAL AND FINAL STATES

Similar to Raman transition (section 7.2.1), the additional initial and final states causes potential leakage out of the three-level system. This limits the minimum time of the transfer in a way similar to that of Raman transition.

### 7.3.3 ADDITIONAL EXCITED STATES

For additional excited states that are farther away than the single photon Rabi frequency  $\Omega_1$  and  $\Omega_2$ , the contribution to the coherent transfer is minimum. However, these states can still contribute to scattering during the transfer.

Excited state will only contribute significantly to the scattering if it causes scattering from the dark state, which happens if  $\Omega_1(t)/\Omega_2(t) \neq \Omega'_1(t)/\Omega'_2(t)$ , where  $\Omega'_1(t)$  and  $\Omega'_2(t)$  are the time dependent single photon Rabi frequencies coupling  $|e'\rangle$  to  $|i\rangle$  and  $|f\rangle$  respectively. Similar to  $\Omega_1$  and  $\Omega_2$ , we can also define  $\Omega'_1 \equiv \max(\Omega'_1(t))$  and  $\Omega'_2 \equiv \max(\Omega'_2(t))$ . Since  $\Omega'_1(t)(\Omega'_2(t))$  and  $\Omega_1(t)(\Omega_2(t))$  are generated from the same beam, we have  $\Omega'_1(t) \propto \Omega_1(t)$  and  $\Omega'_2(t) \propto \Omega_2(t)$  and the condition can also be equivalently expressed as  $\Omega_1/\Omega_2 \neq \Omega'_1/\Omega'_2$ .

More quantitatively, the Rabi frequency coupling the dark state  $|D(t)\rangle$  to the excited state  $|\epsilon'\rangle$  is,

$$\begin{aligned}\Omega'(t) &= \langle \epsilon' | \mathbf{d} \cdot \mathbf{E} | D(t) \rangle \\ &= \frac{\Omega_2(t)\Omega'_1(t) - \Omega_1(t)\Omega'_2(t)}{\sqrt{\Omega_1^2(t) + \Omega_2^2(t)}} \\ &= \frac{\Omega_1(t)\Omega_2(t)}{\sqrt{\Omega_1^2(t) + \Omega_2^2(t)}} \left( \frac{\Omega'_1}{\Omega_1} - \frac{\Omega'_2}{\Omega_2} \right)\end{aligned}$$

The additional scattering caused by this is,

$$\begin{aligned}p'_{scatter} &= \int_0^T \frac{\Gamma'_e \Omega'^2(t)}{4\omega_e'^2} dt \\ &= \frac{\Gamma'_e}{4\omega_e'^2} \left( \frac{\Omega'_1}{\Omega_1} - \frac{\Omega'_2}{\Omega_2} \right)^2 \int_0^T \frac{\Omega_1^2(t)\Omega_2^2(t)}{\Omega_1^2(t) + \Omega_2^2(t)} dt \\ &= C' \frac{\Gamma'_e T}{4\omega_e'^2} \left( \frac{\Omega'_1}{\Omega_1} - \frac{\Omega'_2}{\Omega_2} \right)^2 \frac{\Omega_1^2 \Omega_2^2}{\Omega_1^2 + \Omega_2^2}\end{aligned}$$

which has the form of an off-resonance scattering probability.  $C'$  is a dimensionless number depending only on the pulse shape defined as

$$C' \equiv \frac{\Omega_1^2 + \Omega_2^2}{\Omega_1^2 \Omega_2^2 T} \int_0^T \frac{\Omega_1^2(t)\Omega_2^2(t)}{\Omega_1^2(t) + \Omega_2^2(t)} dt$$

### 7.3.4 CROSS COUPLING BETWEEN LIGHT ADDRESSING INITIAL AND FINAL STATES

As is the case for Raman transition<sup>(7.2.3)</sup>, the coupling of each beam on the other initial or final state can cause increased scattering. The total scattering probability caused by the cross coupling is<sup>‡</sup>,

$$\begin{aligned} p''_{scatter} &= \int_0^T \frac{\Gamma_c \Omega_1^2(t)}{4M_1^2} \frac{M_2^2}{\delta^2} |c_f(t)|^2 + \frac{\Gamma_c \Omega_2^2(t)}{4M_2^2} \frac{M_1^2}{\delta^2} |c_i(t)|^2 dt \\ &= \frac{\Gamma_c}{4\delta^2} \int_0^T \frac{M_2^2}{M_1^2} \frac{\Omega_1^4(t)}{\Omega_1^2(t) + \Omega_2^2(t)} + \frac{M_1^2}{M_2^2} \frac{\Omega_2^4(t)}{\Omega_1^2(t) + \Omega_2^2(t)} dt \\ &= \frac{\Gamma_c T}{4\delta^2} \left( C_1'' \frac{M_2^2}{M_1^2} \frac{\Omega_1^4}{\Omega_1^2 + \Omega_2^2} + C_2'' \frac{M_1^2}{M_2^2} \frac{\Omega_2^4}{\Omega_1^2 + \Omega_2^2} \right) \end{aligned}$$

where  $C_1''$  and  $C_2''$  are two dimensionless numbers depending only on the pulse shape defined as,

$$C_i'' \equiv \frac{\Omega_1^2 + \Omega_2^2}{\Omega_i^4 T} \int_0^T \frac{\Omega_i^4(t) dt}{\Omega_1^2(t) + \Omega_2^2(t)}$$

### 7.3.5 RAMAN TRANSFER VERSUS STIRAP

As one may expect, the scattering probability and the efficiency of a STIRAP transfer depends on the precise pulse shape used. While it may be possible to construct a STIRAP pulse shape, we will focus our discussion on more traditional shapes and assume  $C_1'' \approx C_2'' \approx C' \approx 1$ .

We will compare the scattering probability during STIRAP to that of Raman  $\pi$  pulse in two limiting case depending on whether the contribution from the additional excited or ground state are more significant.

---

<sup>‡</sup>Here we are making the same assumption of identical matrix elements for the two beams as the one we made for Raman transition in section 7.2.3.

## MORE SIGNIFICANT CONTRIBUTION FROM ADDITIONAL EXCITED STATE

This is the case where excited state separation  $\omega'_e$  is significantly smaller compared to the ground state separation  $\delta$ . By choosing an optimal pulse time, the minimum scattering probability for the STIRAP is,

$$\begin{aligned}
 p_{scatter}^{STIRAP} &\approx 2\sqrt{\frac{4\Gamma_e}{\min(\Omega_1^2, \Omega_2^2)} \frac{\Gamma'_e}{4\omega_e'^2} \left(\frac{\Omega'_1}{\Omega_1} - \frac{\Omega'_2}{\Omega_2}\right)^2 \frac{\Omega_1^2 \Omega_2^2}{\Omega_1^2 + \Omega_2^2}} \\
 &= \frac{\sqrt{\Gamma_e \Gamma'_e}}{\omega'_e} \left| \frac{\Omega'_1}{\Omega_1} - \frac{\Omega'_2}{\Omega_2} \right| \frac{2 \max(\Omega_1, \Omega_2)}{\sqrt{\Omega_1^2 + \Omega_2^2}} \\
 &\geq \frac{\sqrt{\Gamma_e \Gamma'_e}}{\omega'_e} \left| \frac{\Omega'_1}{\Omega_1} - \frac{\Omega'_2}{\Omega_2} \right|
 \end{aligned}$$

For Raman  $\pi$  pulse,

$$\begin{aligned}
 p_{scatter}^{RAMAN} &= \frac{\pi\Gamma}{2\Omega_R} \\
 &= \frac{\pi}{2} \frac{\Gamma_e (\Omega_1^2 + \Omega_2^2)}{4\Delta_{max}^2} \frac{2\Delta_{max}}{\Omega_1 \Omega_2} \\
 &= \frac{\pi\Gamma_e}{4\Delta_{max}} \frac{(\Omega_1^2 + \Omega_2^2)}{\Omega_1 \Omega_2} \\
 &\geq \frac{\pi\Gamma_e}{2\Delta_{max}}
 \end{aligned}$$

The last inequality for both take the equal sign when  $\Omega_1 = \Omega_2$ . Comparing the result and note that  $\Delta_{max}$  is a fraction of  $\omega'_e$ , we see that the two scales similarly to the excited state spacing. However, given that in the common cases we have  $\Delta_{max} < \omega'_e$  and  $|\Omega'_1/\Omega_1 - \Omega'_2/\Omega_2| < 1$  using STIRAP

can potentially reduce the total scattering in this case.

#### MORE SIGNIFICANT CONTRIBUTION FROM ADDITIONAL GROUND STATE

With the assumption of  $C_1'' \approx C_2'' \approx 1$  the scattering due to cross coupling for STIRAP is now,

$$\begin{aligned} p_{scatter}'' &= \frac{\Gamma_e T}{4\delta^2} \left( \frac{M_2^2}{M_1^2} \frac{\Omega_1^4}{\Omega_1^2 + \Omega_2^2} + \frac{M_1^2}{M_2^2} \frac{\Omega_2^4}{\Omega_1^2 + \Omega_2^2} \right) \\ &\geq \frac{\Gamma_e T}{2\delta^2} (\Omega_1^2 + \Omega_2^2) \frac{M_1^2 M_2^2}{(M_1^2 + M_2^2)^2} \end{aligned}$$

and the minimum is taken when  $M_2/M_1 = \Omega_2/\Omega_1$ <sup>§</sup> The minimum total scattering rate for STIRAP is therefore,

$$\begin{aligned} p_{scatter}^{STIRAP} &\approx 2 \sqrt{\frac{4\Gamma_e}{\min(\Omega_1^2, \Omega_2^2)} \frac{\Gamma_e}{2\delta^2} (\Omega_1^2 + \Omega_2^2) \frac{M_1^2 M_2^2}{(M_1^2 + M_2^2)^2}} \\ &= 2\sqrt{2} \frac{\Gamma_e}{\delta} \frac{M_1 M_2}{M_1^2 + M_2^2} \frac{\sqrt{\Omega_1^2 + \Omega_2^2}}{\min(\Omega_1, \Omega_2)} \\ &= 2\sqrt{2} \frac{\Gamma_e}{\delta} \frac{\max(M_1, M_2)}{\sqrt{M_1^2 + M_2^2}} \approx 2\sqrt{2} \frac{\Gamma_e}{\delta} \end{aligned}$$

---

<sup>§</sup>Same as Raman transition.



For Raman transition

$$\begin{aligned}
p_{scatter}^{RAMAN} &= \frac{\pi\Gamma}{2\Omega_R} \\
&= \frac{\pi\Gamma_e}{2\Delta} \frac{M_1^2 + M_2^2}{M_1 M_2} \\
&\approx \frac{\pi\Gamma_e}{2\Delta} \frac{\max(M_1, M_2)}{\min(M_1, M_2)}
\end{aligned}$$

we can see that when the single photon Rabi frequency is changed to minimize cross coupling scattering, the Raman transition can be more strongly affected by the matrix element imbalance. However, if the Raman transition can use a detuning

$$\Delta > \frac{\max(M_1, M_2)}{\min(M_1, M_2)} \delta$$

then the scattering probability for a Raman transition can be made smaller than that of STIRAP.

## CONCLUSION

In our experiment, we have an initial and final state separation of  $< 1\text{GHz}$  and an matrix element ratio of  $< 30$ . This means that as long as we can use a single photon detuning of more than  $\approx 30\text{GHz}$ , the total scattering probability for Raman transition will be smaller than that of STIRAP. Since this detuning can be achieved easily, a Raman  $\pi$  pulse should be preferred in our experiment.

The comparison so far has been focused on the scattering probability from the Raman or STI-

RAP beams. There are also a few other more technical reasons we preferred Raman versus STIRAP in our experiment.

1. We use the tweezer beam as the Raman beam for transfer in order to reduce scattering from external sources<sup>6,2</sup>. Doing this for STIRAP while optimizing the pulse shape for transfer is more challenging.
2. In addition to scattering, the additional excited and ground state also causes a power, and therefore time, dependent light shift. A STIRAP in the presence of these shifts must vary the frequency of the two beams in addition to the power in order to maintain the dark state. This is also technically challenging to do.

As a summary, for two photon transfer to a weakly bound molecular state, it is likely that Raman transition is the preferred technique. However, for transferring to a deeply bound molecular state, which is where STIRAP is used in previous experiments, STIRAP can have an advantage over Raman transition.

## 7.4 STATES SELECTION

From section 7.2 we see that the transfer efficiency is directly related to the excited state linewidth, the maximum usable detuning and the matrix elements ratio ( $\mathcal{M}_1/\mathcal{M}_2$ ). In this section, we will discuss how these, as well as other technical constraints affects the choices of states we use for the Raman transfer.

### 7.4.1 INITIAL ATOMIC STATE

The choice of initial state can affect the transfer efficiency by changing the matrix element  $\mathcal{M}_1$  and therefore the matrix elements ratio. Since for most choices of the atomic and molecular states we

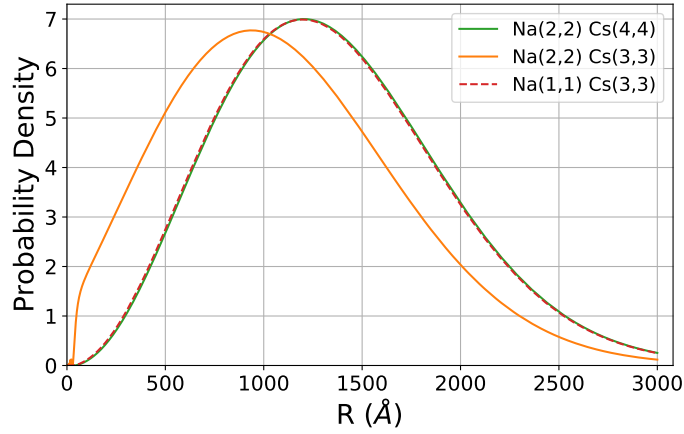


**Figure 7.4:** Enhancement of short range wavefunction. The large scattering length for the  $\text{Na}(2, 2)$ ,  $\text{Cs}(3, 3)$  state creates an interaction shift comparable to the axial trapping frequency. This causes a significant change in the relative wavefunction especially at short intranuclear distance ( $R$ ). Compared to other spin states with weaker interaction, the wavefunction at short distance ( $R < 100\text{\AA}$ ) is significantly enhanced.

have  $M_1 < M_2$ , we would like to choose an atomic initial state with the largest  $M_1$  possible. Unlike the selection of final state (see 7.4.3) maximizing  $M_1$  can improve the matrix element ratio as well as shortening the transfer time to decrease sensitivity to technical noise at the same time.

7.4

#### 7.4.2 EXCITED STATE

Based on theory calculation, most of the molecular excited states have a linewidth  $\Gamma'_e$  very similar to that of the Cesium D lines between  $2\pi \times 5\text{MHz}$  to  $2\pi \times 10\text{MHz}$  due to optical decay process. States above the Cesium  $6^2P_{1/2}$  state, however, could non-radiatively decay to the Cs  $6^2P_{1/2}$  and Na  $3^2S_{1/2}$  states via pre-dissociation which significantly increases the linewidth and should be avoided.

The other factor that affects excited state selection is the maximum detuning. Due to larger FCF with the ground atomic and weakly bound molecular state, previous attempt at Raman spec-

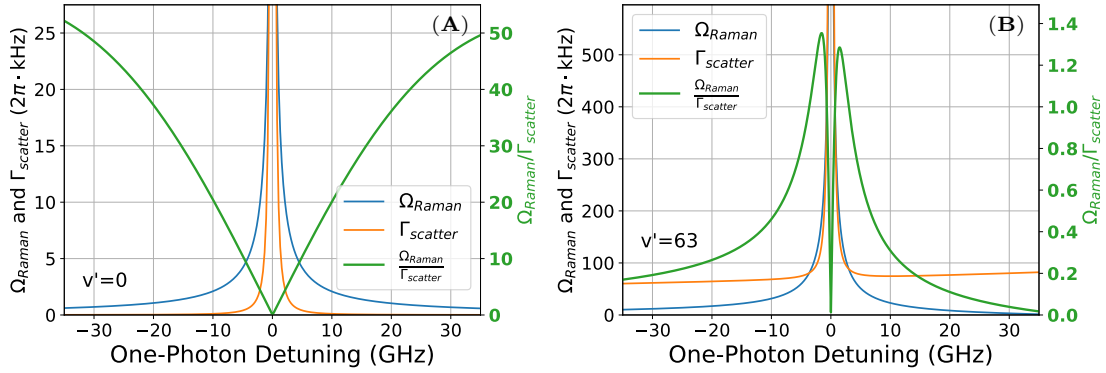


**Figure 7.5:** Comparison between using a weakly bound and a deeply bound excited state as intermediate state for the Raman transition. The (A) deeply bound excited state ( $v' = 0$ ) has a smaller Raman Rabi frequency ( $\Omega_{Raman}$ ) compared to the (B) weakly bound excited state ( $v' = 63$ ) at a given detuning. However, the lower scattering rate ( $\Gamma_{scatter}$ ) allows a much larger  $\Delta_{max}$ , which results in a larger Raman Rabi frequency to scattering rate ratio.

troscopy typically use an excited state closed to the dissociative threshold as the intermediate state.

However, the smaller inter-state spacing and the smaller detuning from the atomic excited state means that these state have a relatively small  $\Delta_{max}$  and therefore a lower coherent transfer efficiency.

On the other hand, a deeply bound excited state has a significantly higher  $\Delta_{max}$  and is the preferred choice for coherent Raman transfer.

In the experiment, we use numerical simulation to calculate the Raman transfer efficiency for any given Raman beam wavelength. Fig. 7.5 shows the result near a deeply bound and weakly bound excited state. Despite having a lower Raman Rabi frequency, the deeply bound state has significantly higher transfer efficiency and is used as the intermediate state for coherent Raman transfer in our experiment.

### 7.4.3 FINAL MOLECULAR STATE

In addition to the scattering and light shift considerations discussed above, the transition can also be affected by external magnetic field. We minimize the effect of magnetic field noise on the transition by using molecular and atomic states that are in the same molecular potential, i.e. molecular bound state in the potential that asymptote to the atomic state. For weakly bound molecular state, i.e. binding energy smaller than or comparable to the hyperfine energy scale, this ensures that the atomic and molecular states have maximally overlapping spin state and therefore a small differential Zeeman shift that can affect the Raman resonance frequency.

Because of the weak coupling between the atomic and molecular states, the Raman transition has a relatively low Rabi frequency. This also means a longer transfer time over which the Raman lasers must remain coherent. In order to lower the requirement on our Raman and tweezer laser, we select the first bound state, i.e. smallest binding energy, as the final molecular state. This ensures the maximum Raman Rabi frequency. Additionally, the typical binding energy for these states are  $< 1\text{GHz}$  which is a frequency difference that can be generated using AOM's so that the coherence between the two beams is greatly improved.

## 7.5 RAMAN TRANSFER RESULTS

### 7.5.1 SCALING OF RAMAN TRANSITION PARAMETERS

## 7.6 CONCLUSION

(outlook:)

Since the final state is mainly selected based on technical considerations, there are other choices that can potentially improve the transfer efficiency. As an example, states with larger binding energies can have weaker coupling to the excited state therefore reducing the matrix elements ratio. Doing so would likely require locking two lasers with a coherence time longer than a few milliseconds.

# 8

## Conclusion



# Computer Control Hardware Specification

NIDAQ

FPGA

DDS

USRP



# B

## Full Raman Sideband Cooling Sequence

Each Raman pulse in the cooling sequence is followed immediately by an optical pumping pulse.

The full parameters for the Raman pulses, including the cooling “axis”, the sideband “order ( $\Delta n$ )”, the cooling frequency “ $\delta'$ ”, the carrier ( $\Delta n = 0$ ) frequency “ $\delta'_0$ ”, the pulse “duration”, the pulse strength in “ $\Omega_0$ ”, and the beam of which a non-uniform “power ramp” is applied, are listed in 6 groups below. The applied cooling frequency,  $\delta'$ , is the two-photon detuning given relative to the

zero-field  $F = 1$  and  $F = 2$  hyperfine splitting of  $1.7716261288(10)$  GHz<sup>Steck</sup>. Due to the Stark shifts of the Raman beams, the carrier transition,  $\delta'_0$ , varies with the power of the Raman beams.  $\delta'_0$  is given also relative to the zero-field hyperfine splitting. The strength of the pulses given in  $\Omega_0$  determines the two-photon Rabi frequency,  $\Omega_{n,\Delta n} = \Omega_0 \langle n | e^{i\vec{k}\cdot\vec{r}} | n + \Delta n \rangle$ . We adopt the convention that a  $\pi$ -pulse between state  $n$  and  $n + \Delta n$  requires a duration  $\pi/\Omega_{n,\Delta n}$ . The difference between  $\delta'$  and  $\delta'_0$  gives the motional sideband frequency,  $\delta$ . Many Raman pulses include a “power ramp” with a Blackman envelope<sup>Kasevich & Chu</sup> to minimize off-resonant excitations. Because each Raman pulse is a product of two spatial- and temporal-overlapped laser beams, the “power ramp” is applied only to the beam that has the smaller light shift (we label the beam by the corresponding  $F$  number) while the other beam has a square-pulse shape. For a Raman pulse with a power ramp, the Rabi frequency gives the arithmetic mean over the duration of the pulse.

## GROUP 1

This group is repeated 4 times.

Axis	$\Delta n$	$\delta'$ (MHz)	$\delta'_0$ (MHz)	Duration ( $\mu s$ )	$\Omega_0$ (kHz)	Power ramp
$x$	-2	19.625	18.649	44.1	$2\pi \times 23$	F <sub>1</sub>
$y$	-2	19.615	18.648	28.6	$2\pi \times 35$	F <sub>1</sub>
$x$	-1	19.130	18.649	36.9	$2\pi \times 23$	F <sub>1</sub>
$y$	-1	19.615	18.648	24.0	$2\pi \times 35$	F <sub>1</sub>

## GROUP 2

This group is repeated 5 times.

Axis	$\Delta n$	$\delta'$ (MHz)	$\delta'_0$ (MHz)	Duration ( $\mu s$ )	$\Omega_0$ (kHz)	Power ramp
$z$	-5	19.030	18.605	81.5	$2\pi \times 16$	F <sub>2</sub>
$x$	-2	19.625	18.649	44.1	$2\pi \times 23$	F <sub>1</sub>
$z$	-4	18.940	18.605	76.3	$2\pi \times 16$	F <sub>2</sub>
$y$	-2	19.615	18.648	28.6	$2\pi \times 35$	F <sub>1</sub>
$z$	-5	19.030	18.605	81.5	$2\pi \times 16$	F <sub>2</sub>
$x$	-1	19.130	18.649	36.9	$2\pi \times 23$	F <sub>1</sub>
$z$	-4	18.940	18.605	76.3	$2\pi \times 16$	F <sub>2</sub>
$y$	-1	19.130	18.648	24.0	$2\pi \times 35$	F <sub>1</sub>

### GROUP 3

This group is repeated 6 times.

Axis	$\Delta n$	$\delta'$ (MHz)	$\delta'_0$ (MHz)	Duration ( $\mu s$ )	$\Omega_0$ (kHz)	Power ramp
$z$	-4	18.940	18.605	76.3	$2\pi \times 16$	F <sub>2</sub>
$x$	-2	19.625	18.649	44.1	$2\pi \times 23$	F <sub>1</sub>
$z$	-3	18.858	18.605	70.2	$2\pi \times 16$	F <sub>2</sub>
$y$	-2	19.615	18.648	28.6	$2\pi \times 35$	F <sub>1</sub>
$z$	-4	18.940	18.605	76.3	$2\pi \times 16$	F <sub>2</sub>
$x$	-1	19.130	18.649	36.9	$2\pi \times 23$	F <sub>1</sub>
$z$	-3	18.858	18.605	70.2	$2\pi \times 16$	F <sub>2</sub>
$y$	-1	19.130	18.648	24.0	$2\pi \times 35$	F <sub>1</sub>

#### GROUP 4

This group is repeated 7 times.

Axis	$\Delta n$	$\delta'$ (MHz)	$\delta'_0$ (MHz)	Duration ( $\mu s$ )	$\Omega_0$ (kHz)	Power ramp
$z$	-3	18.858	18.605	70.2	$2\pi \times 16$	F <sub>2</sub>
$x$	-2	19.625	18.649	44.1	$2\pi \times 23$	F <sub>1</sub>
$z$	-2	18.773	18.605	62.7	$2\pi \times 16$	F <sub>2</sub>
$y$	-2	19.615	18.648	28.6	$2\pi \times 35$	F <sub>1</sub>
$z$	-3	18.858	18.605	70.2	$2\pi \times 16$	F <sub>2</sub>
$x$	-1	19.130	18.649	36.9	$2\pi \times 23$	F <sub>1</sub>
$z$	-2	18.773	18.605	62.7	$2\pi \times 16$	F <sub>2</sub>
$y$	-1	19.130	18.648	24.0	$2\pi \times 35$	F <sub>1</sub>

## GROUP 5

This group is repeated 10 times.

Axis	$\Delta n$	$\delta'$ (MHz)	$\delta'_0$ (MHz)	Duration ( $\mu$ s)	$\Omega_0$ (kHz)	Power ramp
$z$	-2	18.773	18.605	62.7	$2\pi \times 16$	F <sub>2</sub>
$x$	-1	19.130	18.649	36.9	$2\pi \times 23$	F <sub>1</sub>
$z$	-1	18.685	18.605	52.5	$2\pi \times 16$	F <sub>2</sub>
$y$	-1	19.130	18.648	24.0	$2\pi \times 35$	F <sub>1</sub>
$z$	-2	18.773	18.605	62.7	$2\pi \times 16$	F <sub>2</sub>
$x$	-1	19.130	18.649	70.0	$2\pi \times 23$	F <sub>1</sub>
$z$	-1	18.685	18.605	52.5	$2\pi \times 16$	F <sub>2</sub>
$y$	-1	19.130	18.648	46.0	$2\pi \times 35$	F <sub>1</sub>

## GROUP 6

This group is repeated 30 times.

Axis	$\Delta n$	$\delta'$ (MHz)	$\delta'_0$ (MHz)	Duration ( $\mu$ s)	$\Omega_0$ (kHz)	Power ramp
$z$	-1	18.683	18.605	78.7	$2\pi \times 11$	F <sub>2</sub>
$z$	-1	18.683	18.605	135.0	$2\pi \times 11$	F <sub>2</sub>
$z$	-1	18.685	18.605	78.7	$2\pi \times 11$	F <sub>2</sub>
$x$	-1	19.130	18.649	36.9	$2\pi \times 23$	F <sub>1</sub>
$y$	-1	19.130	18.648	24.0	$2\pi \times 35$	F <sub>1</sub>
$z$	-1	18.685	18.605	78.7	$2\pi \times 11$	F <sub>2</sub>
$z$	-1	18.685	18.605	135.0	$2\pi \times 11$	F <sub>2</sub>
$z$	-1	18.685	18.605	78.7	$2\pi \times 11$	F <sub>2</sub>
$x$	-1	19.130	18.649	70.0	$2\pi \times 23$	F <sub>1</sub>
$y$	-1	19.130	18.648	46.0	$2\pi \times 35$	F <sub>1</sub>

# References

- [Docenko et al.] Docenko, O., Tamanis, M., Zaharova, J., Ferber, R., Pashov, A., Knöckel, H., & Tiemann, E. The coupling of the  $X\ 1\ \Sigma^+$  and a  $3\ \Sigma^+$  states of the atom pair Na + Cs and modelling cold collisions. 39(19), S929–S943.
- [2] Grochola, A., Kowalczyk, P., & Jastrzebski, W. Investigation of the  $B\ 1\ \Pi$  state in NaCs by polarisation labelling spectroscopy. 497(1-3), 22–25.
- [3] Grochola, A., Kowalczyk, P., Szczepkowski, J., Jastrzebski, W., Wakim, A., Zabawa, P., & Bigelow, N. P. Spin-forbidden  $c\ 3\ \Sigma^+ (\Omega = 1) \leftarrow X\ 1\ \Sigma^+$  transition in NaCs: Investigation of the  $\Omega = 1$  state in hot and cold environments. 84(1), 012507.
- [Hutzler et al.] Hutzler, N. R., Liu, L. R., Yu, Y., & Ni, K.-K. Eliminating light shifts for single atom trapping. 19(2), 023007.
- [Kasevich & Chu] Kasevich, M. & Chu, S. Laser cooling below a photon recoil with three-level atoms. 69(12), 1741–1744.
- [Kaufman et al.] Kaufman, A. M., Lester, B. J., & Regal, C. A. Cooling a Single Atom in an Optical Tweezer to Its Quantum Ground State. 2(4), 041014.
- [Liu et al.] Liu, L. R., Hood, J. D., Yu, Y., Zhang, J. T., Hutzler, N. R., Rosenband, T., & Ni, K.-K. Building one molecule from a reservoir of two atoms. 360(6391), 900–903.
- [Meekhof et al.] Meekhof, D. M., Monroe, C., King, B. E., Itano, W. M., & Wineland, D. J. Generation of Nonclassical Motional States of a Trapped Atom. 76(11), 1796–1799.
- [Steck] Steck, D. A. Sodium D Line Data.
- [Straughan] Straughan, B. P., Ed. *Spectroscopy. Vol. 3: ...* Number 122 in Science Paperbacks. Chapman and Hall, 2. ed edition.
- [Thompson et al.] Thompson, J. D., Tiecke, T. G., Zibrov, A. S., Vuletić, V., & Lukin, M. D. Coherence and Raman Sideband Cooling of a Single Atom in an Optical Tweezer. 110(13), 133001.



[Zaharova et al.] Zaharova, J., Tamanis, M., Ferber, R., Drozdova, A. N., Pazyuk, E. A., & Stolyarov, A. V. Solution of the fully-mixed-state problem: Direct deperturbation analysis of the  $A\ \Sigma + 1 - b\ \Pi_3$  complex in a NaCs dimer. 79(1), 012508.